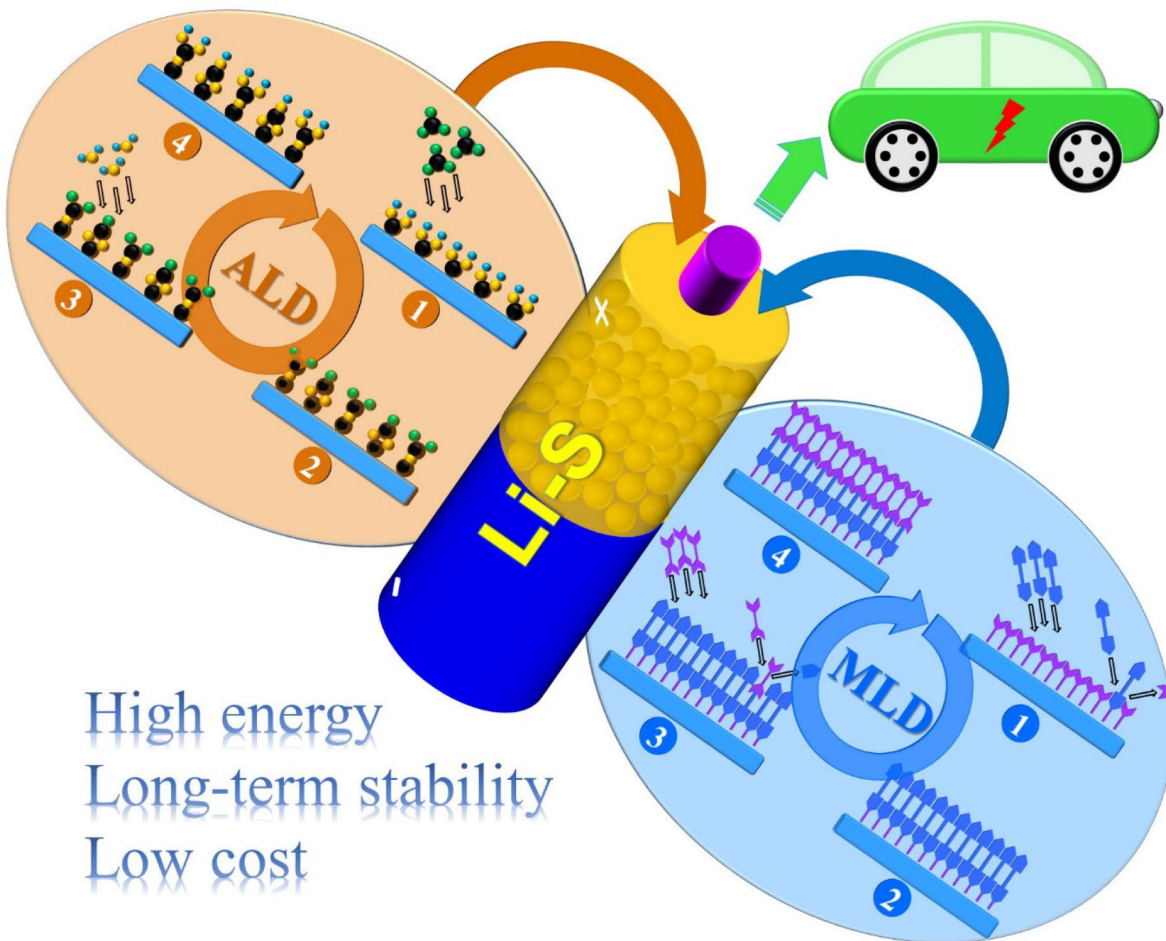




Atomic and Molecular Layer Deposition for Superior Lithium-Sulfur Batteries: Strategies, Performance, and Mechanisms

Qian Sun,^[a] Kah Chun Lau,^{*[b]} Dongsheng Geng,^{*[c]} and Xiangbo Meng^{*[a]}



Lithium-sulfur (Li–S) batteries hold great promise for powering future electric vehicles, given their high theoretical specific energy of 2600 Wh/kg and low cost. However, the commercialization of Li–S batteries is being hindered by several serious technical challenges including the corrosion of lithium metal anodes, the formation of lithium dendrites, the shuttle effect of lithium polysulfides, the decomposition of electrolyte, and low conductivity of sulfur and lithium sulfide. In the past decade, atomic layer deposition (ALD) as a new research thrust has been demonstrated to be a very effective technique in dramatically improving the performance of lithium-ion batteries (LIBs), featuring many unique advantages in fabricating sub-nano to nanoscale inorganic films. Stimulated by ALD's benefits, recently more and more research efforts have been reported in ALD for

addressing the technical issues of Li–S batteries and show very promising outcomes. Analogous to ALD, molecular layer deposition (MLD) is a thin-film technique exclusively for polymeric films. Some of the latest studies have uncovered that MLD is an alternative tool for tackling the challenges of Li–S batteries with exceptional effectiveness. In this review, for the first time, we systematically summarized the progresses of both ALD and MLD in developing superior Li–S batteries, covering their technical strategies, resulting performance, and the underlying mechanisms. In terms of the functionalities of ALD and MLD in Li–S batteries, we focus our discussion in two main complementary aspects: (i) surface coatings and (ii) electrode designs.

1. Introduction

It has been well recognized that limited energy supply,^[1] environmental issues,^[2] and global warming^[3] are among the main concerns in current modern society. Thus, it becomes particularly imperative to widely implement renewable and clean energies for addressing these challenges. Unfortunately, renewable clean energies,^[4] such as wind and solar power, are highly dependent on daily weather conditions, and they only operate intermittently for generating electricity. In this context, electrical energy storage (EES) devices are essential for achieving a continuous energy supply with minimal second-to-second fluctuation. Rechargeable batteries are one of the most promising EES devices and lithium-ion batteries (LIBs) represent the state-of-the-art mainstream technology of rechargeable batteries to date. Since commercialized in 1991 by Sony Corporation,^[5] LIBs now have dominated portable electronics. A standard LIB cell consists of a metal oxide cathode (such as LiCoO_2 , LiFePO_4 , or LiMn_2O_4)^[6] and an anode (such as Li_xC_6 , Li_xSi , or $\text{Li}_4\text{Ti}_5\text{O}_{12}$).^[7] The two electrodes are electrically insulated by a polymeric membrane in a non-aqueous electrolyte (see Figure 1(a)).^[8] A representative electrolyte is a carbonate-based solvent (e.g., ethylene carbonate (EC) or/and diethyl carbonate (DEC)) with a dissolved lithium salt (e.g., lithium bis(trifluoromethanesulfonyl)imide (LiTFSI) or lithium hexafluorophosphate (LiPF₆)). The performance of LIBs, therefore, is dictated by the

adopted anodes, cathodes, and electrolytes.^[9] The interface between an electrolyte and an anode or a cathode also takes a dominant role in determining the performance of LIBs.^[9] Consequently, the achievable energy densities of LIBs are far from their theoretical ones. The state-of-the-art LIBs can typically realize an energy density of 100–220 Wh/kg.^[10] In addition, the issues of LIBs also lie in their cost, safety, and long-term cyclability.^[9] Consequently, LIBs are being hindered from further practical applications in transportation and smart grids. To this end, next-generation LIBs^[11] and new battery prototypes beyond LIBs are proposed and under intensive investigation, such as lithium-sulfur (Li–S) batteries^[12] and lithium-oxygen ($\text{Li}-\text{O}_2$) batteries.^[13] These new battery systems promise much higher energy densities and lower cost. Among the new batteries beyond LIBs, Li–S batteries are particularly attractive. Using lithium metal as the anode and S as the cathode, Li–S batteries are highly regarded as a potentially viable solution to our needs for higher energy, featuring their extremely high theoretical energy density of 2600 Wh/g and the abundant cost-effective S reserve on the earth.^[12] However, Li–S batteries also are experiencing some daunting challenges and these problems should be addressed technically and scientifically before enabling their commercialization on market.^[14]

Herbet and Ulam were among the pioneers proposing elemental sulfur as a cathode material in batteries.^[15] However, the early efforts were not quite successful and disclosed many unpleasant aspects, e.g., the corrosive effect of the aliphatic amines-containing organic electrolyte on cell components and the insolubility of active sulfur materials in the electrolyte. These issues led to the fast capacity fading and low sustainable capacity. Thereafter, there also were a few of research attempts reported for Li–S batteries,^[16] but the progresses were very limited. The recent renaissance of Li–S batteries was stimulated by the work reported in 2009,^[17] in which Nazar and coworkers demonstrated carbon-based sulfur composites being capable of a reversible capacity of 1,320 mAh/g for 20 cycles at a current density of 168 mA/g. Since then, there has been an ever-increasing number of research efforts invested for improving the performance of Li–S batteries.^[18] On one hand, Li–S

[a] Q. Sun, Prof. X. Meng
Department of Mechanical Engineering
University of Arkansas
Fayetteville, Arkansas 72701, USA
E-mail: xbmeng@uark.edu

[b] Prof. K. C. Lau
Department of Physics and Astronomy
California State University Northridge
Northridge, California 91330, USA
E-mail: kahchun.lau@csun.edu

[c] Prof. D. Geng
Center for Green Innovation
School of Mathematics and Physics
University of Science and Technology Beijing
Beijing, 100083, China
E-mail: dgeng@ustb.edu.cn

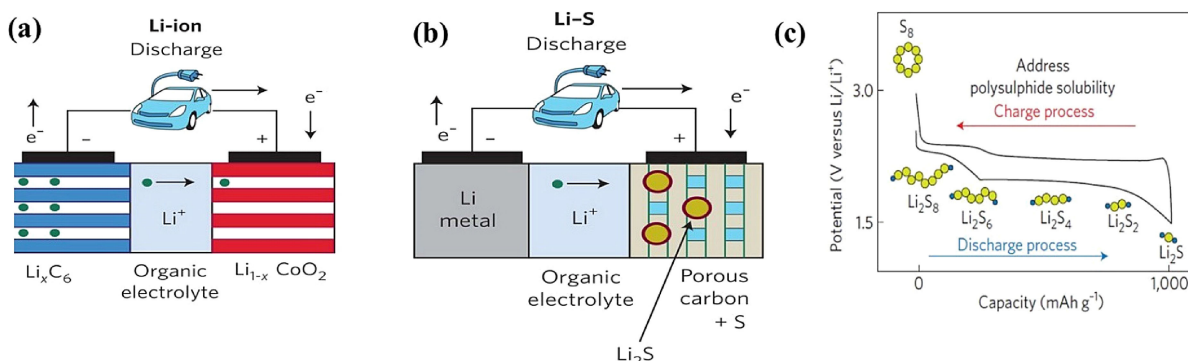


Figure 1. Schematic illustrations of (a) Li-ion and (b) Li–S cells.^[8] (c) Voltage profiles of a Li–S cell.^[8] Reprinted (adapted) with permission from ref. 8. Copyright (2011) Springer Nature.

batteries have a theoretical specific energy of ~2600 Wh/kg, five to ten times higher than the state-of-the-art of LIBs.^[19] On the other hand, sulfur is abundant on the earth, and it is relatively more environmentally friendly and inexpensive.^[12,19e,20] Sulfur widely exists in crude oil, natural gas, and sulfide ores. The elemental sulfur production, for instance, was 9.11 million tons in 2016 in America, while the world sulfur production in all forms was 69.40 and 69.30 million tons in 2015 and 2016, respectively.^[21] The world has an overplus of 3.4 and 3.8 million tons in 2016 and 2017, respectively.^[22] All these make Li–S batteries a cost-effective and high-energy battery technology for powering future electric vehicles.

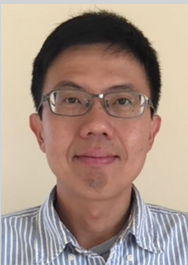
A typical Li–S cell consists of a Li metal anode, an S or Li₂S cathode, an organic solvent with a dissolved lithium salt, and an electronically insulating separator (see Figure 1(b)).^[8] During a discharge process, the sulfur cathode (typically in the form of S₈) undergoes several reduction processes to the final discharge (reduction) product of Li₂S, in which there are several intermediates produced, i.e. Li₂S_n with n=2–8.^[18b] These reactions are reversible in a subsequent charge (oxidation) process. A typical discharge profile of Li–S battery in an ether-based electrolyte (see Figure 1(c))^[8] have two discharge voltage plateaus at 2.2–2.3 V and 1.9–2.1 V, respectively. The higher voltage plateau at 2.2–2.3 V is related to the reduction of elemental sulfur into a high order or long chain soluble lithium



Qian Sun received her B.S. in Applied Chemistry from Shaanxi University of Science and Technology, China in 2013, and M.S. in Chemical Engineering from Northwest University, China in 2016. She worked as a Research Assistant in Zhejiang University in China from June 2016 to December 2016, where she worked on projects of solar energy cells. Currently, she is a graduate student in the group of Professor Xiangbo Meng at University of Arkansas, focusing on interfacial tailoring of lithium batteries using atomic and molecular layer deposition.



Xiangbo (Henry) Meng is an Assistant Professor in the Department of Mechanical Engineering at University of Arkansas (Fayetteville, AR). His research focuses on developing novel nanoscale materials for energy applications such as rechargeable batteries, fuel cells, and catalysis. Dr. Meng was a postdoctoral research fellow in Energy Systems Division at Argonne National Laboratory (2012–2016) and in Chemistry Division at Brookhaven National Laboratory (2011–2012). He earned two PhD degrees in Mechanical & Materials Engineering and Chemical & Biochemical Engineering from the University of Western Ontario (2005–2011). He was an NSERC Postdoctoral Fellow and an awardee of several prestigious honors.



Kah Chun Lau received his PhD degree in Physics from Department of Physics, Michigan Technological University in 2007. He then worked as a postdoctoral fellow at U.S. Naval Research Laboratory and Argonne National Laboratory, also as an Assistant Physicist in Materials Science Division of Argonne National Laboratory. In 2016, he joined the Department of Physics and Astronomy at California State University Northridge as an Assistant Professor. His current research interests focus on the atomistic simulation methods and application in energy related functional materials involved in energy storage and conversion system.



Dongsheng Geng received his PhD degree in Physical Chemistry (including Chemical Physics) from Lanzhou Institute of Chemical Physics, Chinese Academy of Sciences in 2007. He then worked as a postdoctoral fellow at Shinshu University and the University of Western Ontario, and also a research scientist at Institute of Materials Research and Engineering, A*STAR. In 2016, he joined the School of Mathematics and Physics at University of Science and Technology Beijing as a Professor. His current research interests primarily focus on the design, synthesis, and structure-performance correlations of functional materials for electrocatalysis involved in fuel cells and metal-air batteries.

polysulfide, Li_2S_8 , and the subsequent reductions of Li_2S_8 to low order polysulfides Li_2S_n ($3 \leq n \leq 6$), corresponding to the decreasing voltage slope from 2.2 V to ~ 2.1 V. While the lower voltage plateau (1.9–2.1 V) is ascribed to the reductions from the soluble low-order polysulfides (Li_2S_n , $3 \leq n \leq 6$) to the insoluble Li_2S_2 or Li_2S . During the final stage of a discharge process, the reduction from Li_2S_2 to Li_2S is the main reaction step. In a charging process, the discharge product, Li_2S is oxidized and then finally changed into S_8 .

However, Li–S batteries suffer from a series of major challenges in practice.^[20a,f,23] First, the lithium electrode is prone to present heterogeneous deposition and dissolution during charge-discharge processes. In addition, lithium is likely to grow into dendritic structures^[24] and the resulting dendrites pose serious risks to the cell safety. The dendritic lithium is possible to penetrate the separator, reach the cathode side, and then short the cell.^[24e,25] Second, lithium metal anodes tend to experience corrosion in contact with liquid organic electrolytes such as the widely applied mixture of dioxolane (DOL) and dimethoxyethane (DME), leading to the formation of some gaseous and solid by-products, i.e., solid electrolyte interphase (SEI).^[26] The formation of SEI consumes lithium and electrolytes. This may increase cell impedance and lead to the final failure of cells. Third, the intermediates lithium polysulfides (Li_2S_n , $3 \leq n \leq 8$) are highly soluble in liquid electrolytes, and thereby enable shuttling freely between the sulfur cathode and the lithium anode. The S shuttling renders self-discharge, low Coulombic efficiency (CE), faded capacity, and loss of active sulfur.^[27] Fourth, both S and Li_2S are highly insulating electrically and ionically, accounting for about 5×10^{-30} S/cm at 25 °C.^[28] Fifth, there is a large volume change ($\sim 80\%$) during the redox process of S/ Li_2S .^[29] This may potentially hinder the sulfur active materials from intimately contacting with the cathode current collector.

Aimed at overcoming the afore-discussed issues, in the past decade, researchers have conducted a huge amount of studies with various strategies. In addressing the insulating nature of S and Li_2S , for instance, different types of novel carbon materials have been chosen as additives^[30] to improve the electrical conductivity of S cathode materials. Metal oxides were developed as adsorbents of polysulfides to mitigate the S shuttling, such as TiO_2 ,^[31] Ti_4O_7 ,^[32] indium tin oxide,^[33] Al_2O_3 ,^[34] SiO_2 ,^[23a] La_2O_3 ,^[35] and $\text{Mg}_{0.6}\text{Ni}_{0.4}\text{O}$.^[36] In addition, solid electrolytes,^[37] electrolyte additives,^[23c,38] and ionically conductive polymers^[39] were also explored to improve the performance of Li–S batteries. Among the many efforts, in the past five years atomic layer deposition (ALD) has appeared as a new technique for tackling these challenges of Li–S batteries. There were two technical strategies of ALD reported to date: (i) surface modifications of S/ Li_2S and metallic lithium electrodes and (ii) new S/ Li_2S electrode designs. Following the emerging ALD efforts, molecular layer deposition (MLD) has also been initiated for developing high-performance Li–S batteries. MLD is a technique analogous to ALD but exclusively for organic and inorganic-organic hybrid materials.^[40] Ascribed to their unique thin-film growth mechanism and characteristics, both ALD and MLD nearly enable any inorganic and organic materials with

high controllability at the atomic and molecular level,^[40,41] respectively. In addition, ALD and MLD techniques distinguish themselves from traditional solution-based methods^[42] in producing conformal and uniform sub-nanometer thin films over complex and large-scale planar substrates at low temperatures. All these benefits have led to the recently expanding applications of ALD and MLD in battery research, as documented in literature.^[40,43] Thus, ALD and MLD have been recognized as two very powerful and promising techniques for new battery systems, and have been attracting more and more research enthusiasms for many newly emerging applications.^[40,44]

Stimulated by the recent progresses, we herein for the first time contribute this comprehensive survey highlighting the unique functional roles of ALD and MLD in Li–S batteries. Following this introductory section, we give a brief introduction on both ALD and MLD techniques. Then, we focus on discussing the effectiveness of the surface coatings of ALD and MLD for high-performance Li–S batteries in the third section. The ALD and MLD coatings are summarized for improving both S cathodes and Li metal anodes. In the fourth part, we summarize the ALD's work in designing new electrodes of Li–S batteries. In the last part, we conclude this summary with some outlooks. With this review, we expect that there will be more research efforts boosted in utilizing ALD and MLD for superior Li–S batteries and other battery systems.

2. An Overview on ALD and MLD

ALD is a thin film technique based on a self-limiting growth mechanism.^[43d,e,45] Initially coined as “atomic layer epitaxy (ALE)” by Suntola et al. in the 1970s,^[46] ALD has been bearing the name “atomic layer deposition” since the beginning of the 21st century, when it was discovered to have great potentials for nanoscience and nanotechnology. Originally invented for semiconductor industries, ALD now has greatly expanded its applications into catalysis,^[47] renewable clean energies (e.g., batteries, solar cells, fuel cells, supercapacitors, and water splitting),^[43a,d,e,48] biomedical,^[49] surface engineering,^[50] and many others.^[51] All these are owing to ALD's distinguished capabilities in synthesizing novel materials at the atomic level. To date, ALD has produced a large variety of inorganic materials, covering elements,^[52] metal oxides,^[41,c,53] metal sulfides,^[44] metal nitrides,^[52a] metal fluorides,^[54] and complex compounds.^[55] The unique mechanism of ALD can be exemplified using a process of metal oxides (e.g., Al_2O_3) (see Figure 2(a)).^[40] Typically, four steps are included: (i) a supply of the metal precursor, e.g., trimethylaluminum (TMA); (ii) a full purge to clean the oversupplied metal precursor and any byproducts, i.e., TMA and methane; (iii) a supply of the oxygen precursor, e.g., water; and (iv) another full purge to clean the oversupplied oxygen precursor and any new byproducts, i.e., water and methane. Each supply of the two precursors initiates a self-terminating surface reaction and the two surface reactions together result in a layer growth of the target material, e.g., Al_2O_3 . In particular, this four-step process is cyclic and this

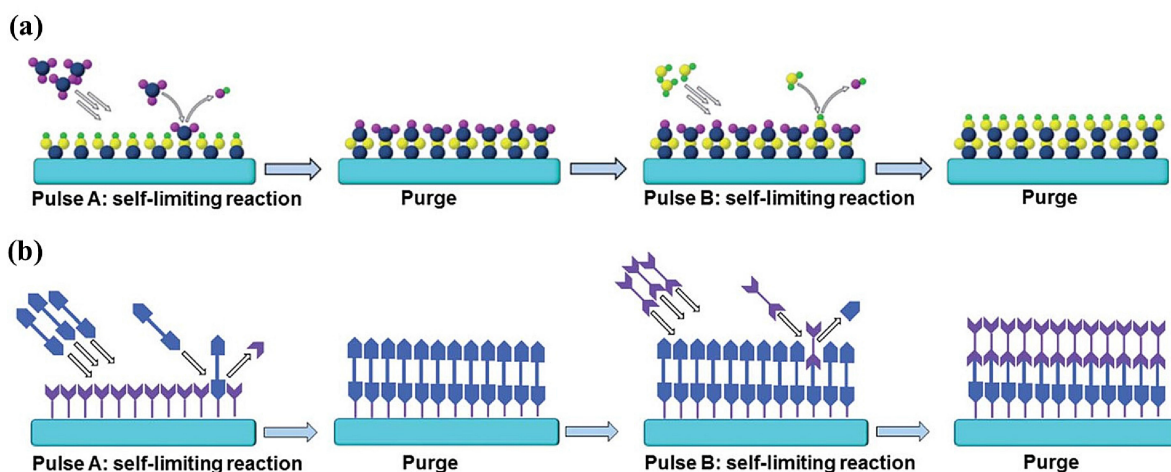


Figure 2. Illustrations of (a) an ALD process and (b) a MLD process.^[40] Reprinted (adapted) with permission from ref. 40. Copyright (2017) Royal Society of Chemistry.

makes ALD a precisely controllable layer-by-layer growth technique at the atomic scale. Furthermore, it is important to point out that ALD processes are generally dictated by three key parameters, i.e., temperature, substrate, and precursor.^[43e] Smart selections on these three parameters are essential for producing any desirable materials with an optimal growth. Readers may refer to many excellent reviews for information, as well documented in literature.^[41a,56]

Analogous to ALD enabling inorganic materials, MLD shares a very similar growth mechanism exclusively for organic or organic-inorganic hybrid materials, which was firstly coined in 1991 by Yoshimura et al. for producing polyimide polymer film.^[57] So far, MLD has succeeded in preparing many types of polymeric films (e.g., polyurea, polyamide, polythiourea, polyurethane, polyazomethine, and polyester films)^[58] and organic-inorganic hybrid materials (e.g., alucone, zincone, titanocene, zirconium, and hafnicones),^[59] as recently reviewed by Meng.^[40] A typical MLD process also consists of four steps, i.e., two precursor supplies and two full purges, as illustrated in Figure 2(b).^[40] In this regard, several excellent reviews can provide more detailed information.^[40,60] In summary, ALD and MLD share many common characteristics: excellent uniformity on large-scale planar substrates, unrivaled conformality over complex high-aspect-ratio substrates, highly controllability over material growth processes, low growth temperature, and flexible tunable film properties. However, MLD is superior to ALD in the resultant organic materials' flexibility and this is very important for applications requiring materials with exceptional elasticity. For example, as recently reviewed,^[61] MLD offered new options of organic coating materials for addressing the issues of Si anodes in LIBs, since Si has been suffering from an extremely high volume change of 300% during charge-discharge cycling. Organic coatings have been demonstrated being beneficial to sustain the integrity of Si particles.^[62] Commonly, the general benefits of ALD and MLD mainly lie in several aspects: (i) accurately controlled ultrathin films at the nanoscale, (ii) unrivaled conformal and conformal coatings, (iii)

low growth temperature even down to room temperature, and (iv) the only techniques to date enabling direct coatings over electrodes.^[43b,e,61]

Given the many benefits of ALD and MLD in batteries, Meng et al.^[43e] has made the first summary about ALD for LIBs in 2012. In 2017, Meng has contributed to another overview on ALD for sodium-ion batteries.^[43b] Furthermore, recently Meng also has given a comprehensive account on the mechanism, growth characteristics, and promising applications of MLD.^[40] The three reviews jointly demonstrate that ALD and MLD are two very powerful and effective techniques offering viable strategies against the challenges in battery systems, enabling surface coatings, electrode designs, and development of solid-state electrolytes. With the ever-growing interests in high-energy and cost-effective Li–S batteries, it will be very helpful to have a thorough survey on the recent efforts of ALD and MLD in Li–S batteries. To this end, therefore, we are prompted to summarize the ALD and MLD studies reported to date for Li–S batteries, specially highlighting the effects of surface coatings and electrode designs via both ALD and MLD.

3. Surface Coatings via ALD and MLD

3.1. Surface Coatings via ALD

3.1.1. Sulfur Cathodes

As discussed above, S/Li₂S cathodes pose several big challenges to the practice of Li–S batteries, i.e., their insulating nature, highly soluble intermediate products (Li_nS_n, 3 ≤ n ≤ 8), and 80% volume change during electrochemical processes. Among these issues, the shuttling of polysulfides is particularly notorious. In this regard, the recent studies have shown that ALD can offer new strategies to inhibit the dissolution and shuttling of lithium polysulfides, improve CE, and help sustain high capacity of S/Li₂S cathodes during cell cycling.

Kim et al. conducted the first study of applying ALD- Al_2O_3 on S cathodes.^[63] In their study, sulfur was infiltrated into activated carbon fibers (ACFs) at 120 °C. After the infiltration, S deposited outside the ACFs was removed at 230 °C. In the resultant S-ACF composites, ACFs were used as the host material of the infiltrated sulfur. The S-ACF composites were fabricated into cathodes and the prepared S-ACF cathodes were further coated with Al_2O_3 using plasma-enhanced ALD (i.e., PE-ALD using TMA and O_2 plasma as precursors) for 30 and 50 ALD cycles (denoted as 30- Al_2O_3 and 50- Al_2O_3 , respectively). In comparison to the bare S-ACF cathode, the S-ACF cathodes with ALD- Al_2O_3 coatings exhibited evident increases in sustainable capacity after 150 discharge-charge cycles at an elevated temperature of 70 °C. The electrochemical evaluations at 70 °C was for promoting the dissolution of lithium polysulfides in the S-ACF cathodes. The subsequent electrochemical investigation further revealed that, among the three cathodes, the bare S-ACF cathode delivered a high capacity of 932 mAh/g initially (see Figure 3(a)), but experienced a rapid capacity fading because of the repetitive dissolution and re-deposition of polysulfides. Consequently, the bare S-ACF cathode sustained a capacity of 300 mAh/g after 150 cycles (see Figure 3(b)). It was believed that the existence of LiNO_3 in the electrolyte must have resulted in the formation of a thick SEI layer on the lithium metal anode, and the SEI therefore has alleviated the deposition of the insulating lithium sulfides (Li_2S or/and Li_2S_2) on the metallic lithium anode. In contrast to the bare S-ACF cathode, the two ALD-coated S-ACF cathodes both exhibit much lower

initial capacities in the range of 370–420 mAh/g (see Figure 3(a)). This was probably caused by the low lithium ionic diffusion rate related to the insulating ALD- Al_2O_3 coatings, but the cathodes with Al_2O_3 coatings exhibited a dramatic increase of capacity to 500–650 mAh/g after 150 cycles (see Figure 3(b)). Subsequently, both the Al_2O_3 -coated cathodes exhibited a decay of capacity after 270–370 cycles (see Figure 3(b)), probably attributed to the accumulated SEI formation at the high temperature of 70 °C and the uncontrolled electrochemically active polysulfide dissolution from the cathodes. In examining the discharge profiles of the three cathodes, it was disclosed that the bare S-ACF cathode has an increased polarization after several cycles while the two ALD coated cathodes have alleviated the polarization. After 100 cycles, the cell polarization was significant for all the three cells, suggesting that Li ion diffusion has been seriously hindered due to the deposition of Li_2S_2 as well as the formation of thick SEI layer. After 300 cycles, the bare S-ACF cathode exhibited a nearly negligible capacity, while the two ALD-coated cathodes still could sustain a decent capacity of > 500 mAh/g. SEM (scanning electron microscopy) observation also provided evidence on the effects of ALD-coatings. Based on the cycled cathodes, it was found that the bare S-ACF cathode (see Figure 3(c)) was coated by large chunks of irregular insulating lithium sulfides particles, while the ALD-coated cathodes (see Figure 3(d)) were not covered by these large insulating particles. This was also verified by the S elemental mapping using energy-dispersive X-ray spectroscopy (EDX) (see Figure 3(e)).

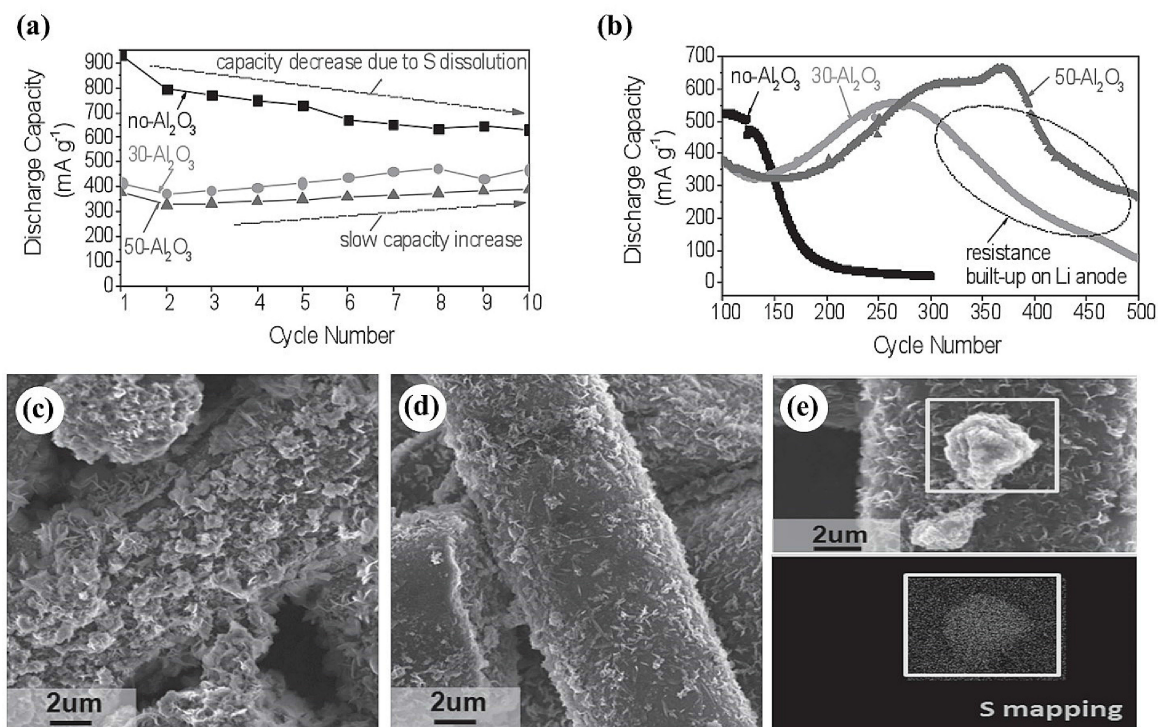


Figure 3. The impact of alumina coatings on electrochemical performance of S-ACFs electrodes at an elevated temperature of 70 °C.^[63] The discharge capacity of the electrodes at a current density of C/5: (a) initial and (b) long-term performance. Capacity is normalized by the weight of S. SEM results of (c) the bare S-ACF and (d) 50- Al_2O_3 coated S-ACF electrodes after 200 cycles. (e) EDX S-mapping of large particles on bare S-ACF. Reprinted (adapted) with permission from ref. 63. Copyright (2013) John Wiley and Sons.

Following the study by Kim et al., a similar work was conducted by Yu et al.,^[6] in which ALD-Al₂O₃ was used to coat graphene-based sulfur composite (i.e., G–S). Yu et al. prepared the G–S composite through hydrothermally reducing graphene oxides (GO, fabricated via an improved Hummers method) with CS₂. The G–S aerogel was cut and pressed into circular plates for cell assembly (see Figure 4(a)). ALD coatings were performed on the resultant pellets for 5 and 10 cycles (i.e., G–S-5 and G–S-10, respectively) using TMA and water as precursors. With the increased electrochemical cycling number, the cyclic voltammograms (CV) curves of the bare G–S electrode had irregular peaks, while that of the G–S-10 electrode exhibited a stable electrochemical profile, implying that the uniform Al₂O₃ coating was favorable to reduce the dissolution of lithium polysulfide and to increase the stability of the G–S composite. Furthermore, the capacity of the bare G–S electrode was 697 mAh/g initially, but dropped to 314 mAh/g after 100 cycles (see Figure 4(b)). This might be due to the severe lithium polysulfide dissolution. In contrast, both the G–S-10 and G–S-5 cathodes exhibited much higher initial capacities (795 and 780 mAh/g, respectively), and could still sustain 625 and 470 mAh/g after 100 cycles, respectively. The capacity retention was 82%, 69%, and 45% for the G–S-10, the G–S-5, and the bare G–S electrode, respectively. In addition, the CEs of G–S-10 and G–S-5 were 93% and 88%, respectively, much higher than that of the bare G–S electrode (80%). SEM observations also

revealed that the bare G–S cathode was covered by many lumps of non-uniform insoluble lithium sulfides after 100 discharge-charge cycles (see Figure 4(c)), while the G–S-10 cathode had a much smoother microporous structure free of big lumps (see Figure 4(d)). All these consistently evidence that the ALD coatings could effectively inhibit the shuttling behaviors of lithium polysulfides and therefore help realize improved performance. Yu et al.^[6] believed that the benefits of the ALD-coated G–S cathodes lied in two aspects: (i) ALD coatings served as kinetic barriers to avoid the full contact of both the electrochemical active S species and carbon defect sites with liquid electrolytes, and therefore reduced unwanted parasitic reactions, and (ii) the porous graphene networks helped accommodate the volume change of S active species while improved the cathodes' electrical conductivity.

In an effort for high-loading S cathodes up to 65 wt.% S, Meng et al. developed a cost-effective ball-milling process (see Figure 5(a)).^[64] In the work, Meng et al. first clarified that, in comparison to micro-sized S particles, the nanophase S particles prepared from the ball milling are beneficial for achieving higher CE and capacity. To further improve the performance of the nanophase sulfur cathodes, Meng et al. deposited ALD Al₂O₃ coatings on the nanophase S cathodes with various ALD cycles, i.e., 5, 10, 20, 50, and 100 at a low temperature of 50 °C using TMA and H₂O as precursors. In their work,^[64] the low ALD deposition temperature of 50 °C was confirmed being very

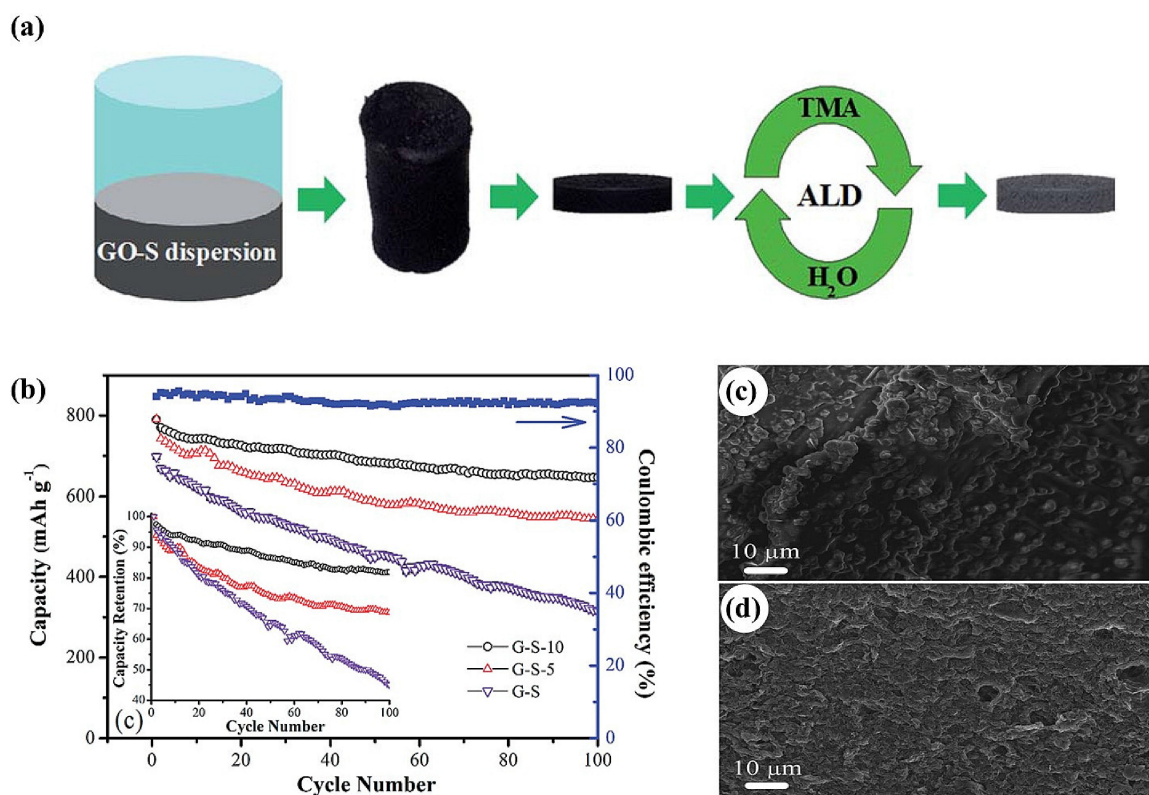


Figure 4. (a) Schematic illustration of the preparation of G–S composites coated with Al₂O₃ by ALD. (b) The cycling performance of the G–S composite electrodes with or without an Al₂O₃ coating at a constant rate of 0.5 C. The typical Coulombic efficiency of the G–S-10 electrode is shown. The inset shows the capacity retention of the corresponding electrodes upon cycling. Morphologies of (c) G–S and (d) G–S-10 composite electrodes after 100 cycles at 0.5 C.^[6] Reprinted (adapted) with permission from ref. 6. Copyright (2014) Royal Society of Chemistry.

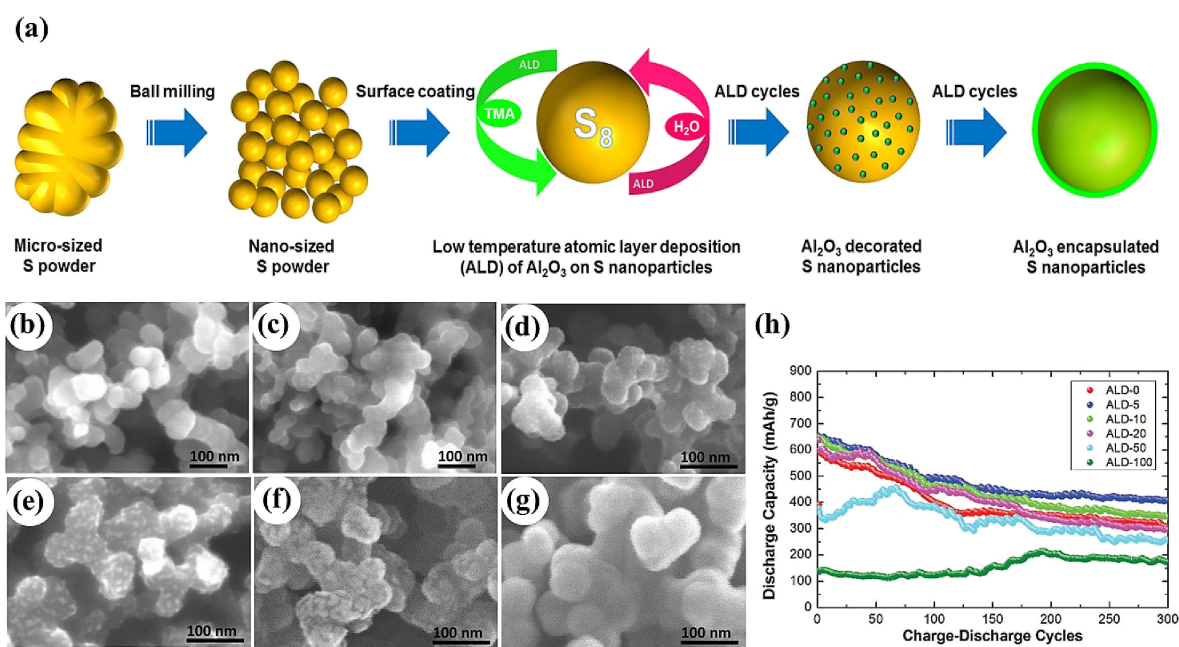


Figure 5. (a) Schematic illustration of two methodologies used for high-performance Li–S batteries: (i) mechanical grinding via ball milling and (ii) low temperature atomic layer deposition of Al_2O_3 . SEM images for (b) the pristine S cathode and the ALD-coated S cathodes with (c) 5, (d) 10, (e) 20, (f) 50, and (g) 100 cycles of Al_2O_3 ALD. (h) Electrochemical performance of the S cathodes at a current density of $200 \text{ mA}\text{h g}^{-1}$: the discharge capacity of S electrodes versus number of charge-discharge cycles.^[64] Reprinted (adapted) with permission from ref. 64. Copyright (2017) John Wiley and Sons.

effective for mitigating the S sublimation during the ALD processes. They differentiated the nanophase S cathodes with ALD coatings, i.e., $S_{\text{ALD}-x}$ ($x=0, 5, 10, 20, 50$, and 100 ALD cycles). Meng et al. revealed that the ALD Al_2O_3 coatings exhibited different coverages on S cathodes (see Figure 5(b–g)), i.e., dispersed nanoparticles (5–20 ALD cycles), porous nanofilms (50 ALD cycles), and uniform dense nanofilms (100 ALD cycles). Very interestingly, Meng et al. for the first time discovered that there are two fundamentally different mechanisms underlying the effects of the ALD Al_2O_3 coatings in improving the performance of the resultant S cathodes. In the case of low ALD cycles (e.g., ≤ 20 cycles), Al_2O_3 existed as dispersed nanoparticles on the S cathodes and performed as exceptional absorbents to polysulfides. In the case of high ALD cycles (e.g., ≥ 50 cycles), Al_2O_3 formed an integral film over S cathodes and acted as a physical barrier to inhibit polysulfides from contacting and dissolving in liquid electrolytes. In terms of sustainable capacity, Meng et al. revealed that $S_{\text{ALD}-5}$ exhibited the highest discharge capacity of 408 mAh/g after 300 cycles (see Figure 5(h)), accounting for 57.8% higher than that of the bare nanophase S cathode (i.e., $S_{\text{ALD}-0}$). In the case of $S_{\text{ALD}-100}$, the electrochemical reactions of the S cathode were restricted, due to the uniform dense coating of insulating Al_2O_3 . Thus, $S_{\text{ALD}-100}$ showed a very limited capacity. However, $S_{\text{ALD}-100}$ exhibited the highest CE. This study confirmed that both the complementary strategies via selective chemical adsorption and physical barrier are viable for inhibiting the shuttling of soluble polysulfides in Li–S cell. This work clearly indicates that a well-controlled ALD coating is a very promising approach to fine-tune electrode surface for the optimal performance of Li–S batteries.

In addition to S cathodes, recently there was also a study on applying ALD coatings on Li_2S cathodes. In the work, as illustrated in Figure 6(a), Chen et al.^[65] infused Li_2SO_4 solution into a graphene oxide sponge (GS) via a vacuum process. A subsequent thermal process turned the Li_2SO_4 -GS into Li_2S -GS composites. The Li_2S -GS composites were then coated by ALD Al_2O_3 using TMA and O_3 as precursors at 120°C . Chen et al.^[65] found that a layer of 1-nm ultra-thin Al_2O_3 coating could not only strongly interact with lithium polysulfides via $\text{Li}-\text{O}$ bonds, but also physically block lithium polysulfides from dissolution. Electrochemical testing revealed that the resultant Al_2O_3 - Li_2S -GS cathode had an initial capacity of 866 mAh/g and still maintained a high capacity of 736 mAh/g after 150 cycles, accounting for a retention rate of 85% . In comparison, the bare Li_2S -GS cathode exhibited a relatively low initial specific capacity of 824 mAh/g , but experienced a serious capacity fading to remain a capacity of 500 mAh/g after 150 cycles. Apparently, the ALD- Al_2O_3 coating had greatly improved the performance of the Li_2S -GS cathodes by inhibiting polysulfide shuttling. After 150 cycles, the bare Li_2S -GS electrode was covered with many lumps related to Li dendrites and insoluble lithium sulfides. In contrast, the ALD- Al_2O_3 coated Li_2S -GS cathode showed a much smoother surface. A long-term cycling test further verified that the Al_2O_3 - Li_2S -GS cathode realized an initial capacity of 420 mAh/g and still maintained a high capacity of 373 mAh/g after 300 cycles at 0.5 C , having an average CE of 99% during cycling (see Figure 6(b)). In addition, the Al_2O_3 - Li_2S -GS cathode exhibited a good rate capability (see Figure 6(c)) at different current densities. Chen et al.^[65] believed that the improved performance of the Al_2O_3 - Li_2S -GS cathode lied in three aspects: (i) a 3D porous structure of Al_2O_3 - Li_2S -GS

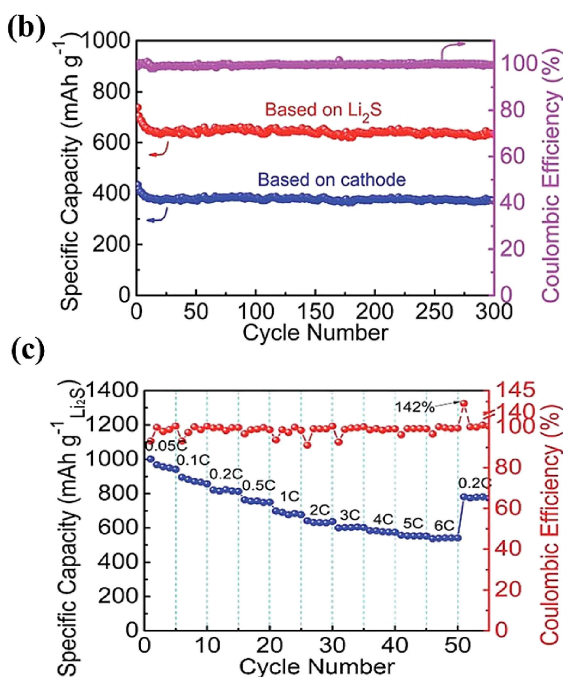
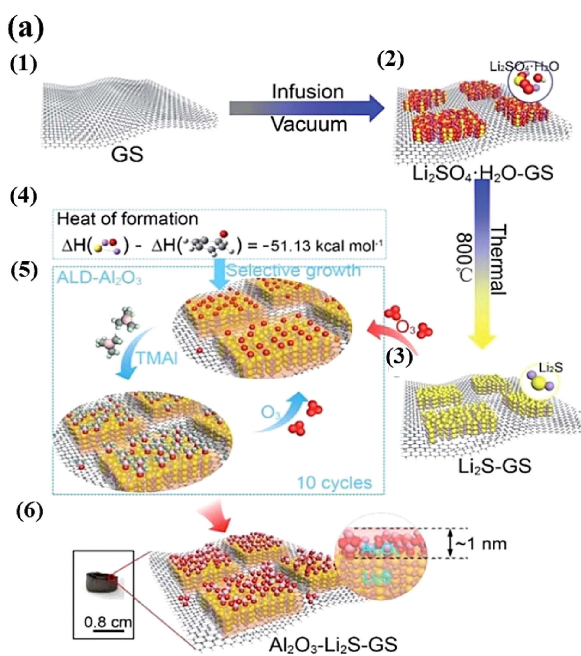


Figure 6. (a) Schematic of Al_2O_3 - Li_2S -GS composite synthesis: (1–3 and 6) steps involved in the synthesis process, (4) heat of formation of graphene-O and Li_2S -O calculated by the first-principles calculations, and (5) schematic during Al_2O_3 -ALD cycles. (b) Electrochemical performance of Al_2O_3 - Li_2S -GS cathodes at 0.5 C and (c) rate in the range of 0.05 C to 6 C.^[65] Reprinted (adapted) with permission from ref. 65. Copyright (2016) Royal Society of Chemistry.

cathode enabled fast transport of Li^+ ; (ii) the direct deposition of Al_2O_3 on Li_2S particles rather than on rGO helped maintain the good electric conductivity of rGO; and (iii) the ultrathin ALD Al_2O_3 film was capable of suppressing the lithium polysulfides from dissolution.

Additionally, Luo et al.^[66] conducted a research on modifying carbonized mesoporous wood fibers using ALD- Al_2O_3 . Natural wood fibers were selected to be a promising material for hosting sulfur, since they have a hierarchical mesoporous structure (see Figure 7(a2)). The natural wood fibers were carbonized at high-temperature (see Figure 7(a3)) to obtain mesoporous carbon fibers (see Figure 7(a4)). Subsequently, a layer of 5-nm thick Al_2O_3 coating was applied on the carbonized mesoporous wood fibers (CMWFs) via an ALD process at 150 °C using TMA and water as precursors to generate a functionalized CMWFs (f-CMWFs, see Figure 7(a5)). Due to its vapor phase, the ALD- Al_2O_3 could deposit into small pores of CMWFs to reduce their sizes and volumes. Using a sealed vacuum glass tube technique, elemental sulfur was infiltrated into f-CMWFs to obtain S/f-CMWFs (see Figure 7(a6)). Besides featuring a high sulfur loading of 70 wt %, the obtained S/f-CMWFs (see Figure 7(a6)) is also a current collector-free, binder and additives-free cathode for Li–S batteries.^[66] The porous natural wood fiber after carbonization was well preserved to ensure the electron transfer. Moreover, there were numerous small pores existing in the CMWFs that could also serve as electrolyte reservoirs in the Li–S battery. The ALD- Al_2O_3 was used to reduce the pore size of CMWFs for better trapping polysulfides.^[66] Brunauer–Emmett–Teller (BET) results indicated that f-CMWF exhibited a specific surface area of 586 m²/g and pore volume of 0.27 cm³/g, while the S/f-CMWF has a smaller surface area of

159 m²/g and pore volume of 0.0798 cm³/g, which was ascribed to the influence of sulfur infiltration during the synthesis process. It was also concluded that the mesopores smaller than 5 nm would enable encapsulating redox active sulfur species in the conductive carbon matrix. In the study,^[66] thermogravimetric analysis (TGA) was conducted to determine the sulfur content in CMWF and f-CMWF, accounting for 76% and 70%, respectively. In addition, X-ray diffraction (XRD) measurements demonstrated that there were no sharp peaks for both CMWF and f-CMWF, implying their amorphous nature. In contrast, there were some sharp XRD peaks for sulfur after sulfur infiltration into mesoporous carbon. Electrochemical testing disclosed that, as shown in Figure 7(b), the S/CMWF cathode exhibited three discharge voltage plateaus at 2.35, 2.05, and 1.55 V, while two charge voltage plateaus at 2.1 and 2.4 V. In comparison, S/f-CMWF showed only one discharge voltage plateau at 1.65 V and one charge voltage plateau at 2.1 V, implying that most of the sulfur was confined in the mesopores (see Figure 7(c)). Electrochemical results revealed that the S/CMWF electrode could achieve a capacity of 1246 mAh/g initially and faded dramatically to 442 mAh/g after 30 cycles. In contrast, the S/f-CMWF electrode delivered an initial capacity of 1115 mAh/g and maintained a high capacity of 859 mAh/g after 450 cycles. Luo et al.^[66] believed that the improved performance of the S/f-CMWF electrode was related to the ALD- Al_2O_3 layer, which had reduced the pore size of CMWF and thereby helped effectively prevent the polysulfides from shuttling. Luo et al.^[66] also demonstrated that the S/f-CMWF electrode had exceptionally high rate capability, accounting for a capacity of 1000 mAh/g at a high current density of 100 mA/g and 430 mAh/g at 4 A/g. Luo et al.^[66] believed that the high conductivity of the f-

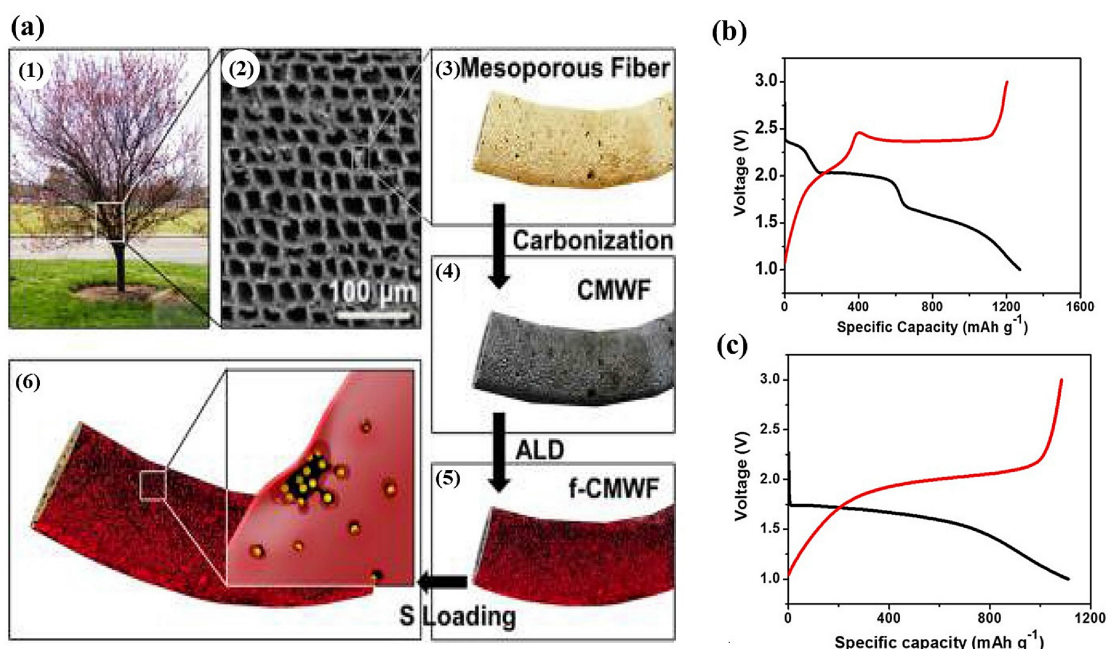


Figure 7. (a) Schematic of the hierarchical and mesoporous structure of natural wood fiber: (1) a picture of tree, (2) the cross-sectional SEM image of wood trunk, (3) the schematic of a single wood fiber (The gray color indicates the mesopores along the fiber), (4) the schematic of the CMWF after carbonization, (5) the schematic of the f-CMWF with ALD Al₂O₃ (The red color indicates Al₂O₃), and (6) the schematic of sulfur infiltration in the Al₂O₃ coated f-CMWF (The yellow spheres represent sulfur). Al₂O₃ is deposited at the interface between carbon and sulfur. The small molecular sulfur is encapsulated within the carbon mesopores. Galvanostatic charge/discharge profiles of (b) S/CMWF electrode and (c) S/f-CMWF electrode.^[66] Reprinted (adapted) with permission from ref. 66. Copyright (2017) American Chemical Society.

CMWF and its meso- and microporous structure might have played some important roles for achieving the high performance of S/f-CMWF.

Following the efforts in ALD-Al₂O₃ discussed above, researchers also explored the effects of some other ALD coatings. Yu et al.^[67] have investigated the effects of ALD-ZnO and ALD-MgO coatings of 40 ALD cycles on reduced graphene oxide-sulfur (G-S) composite pallets (see Figure 8(a–c)), named as ZnO/G-S and MgO/G-S, respectively. The cyclability of the bare G-S, ZnO/G-S, and MgO/G-S are illustrated in Figure 8(d). The bare G-S electrode showed an initial discharge capacity of 1120 mAh/g, but the capacity continuously decreased with electrochemical cycles and remained 700 mAh/g at the 100th cycle. In comparison, the ZnO/G-S cathode started from an initial capacity of 949 mAh/g, increased to 998 mAh/g in the first several cycles (probably ascribed to the improved wetting and activation of the electrode), and sustained a capacity of 845 mAh/g at the 100th cycle. The MgO/G-S cathode exhibited an initial capacity of 923 mAh/g, increased slightly in the first 10 cycles, and remained a capacity of 767 mAh/g at 100th cycle. In addition, the capacity retention is 63%, 89%, and 83% for the bare G-S, ZnO/G-S, and MgO/G-S, respectively. Among the three cathodes, the ZnO/G-S achieved the highest CE of 92% and the highest capacities of 826, 712 and 581 mAh/g at 0.5, 1 and 2C, respectively. Yu et al.^[67] suspected that a large amount of –OH groups was associated with the ZnO coating and they might have helped trap polysulfide anions. Yu et al.^[67] also conducted a study to address the interactions of lithium polysulfides with oxides, using the density functional theory

(DFT) calculations. Yu et al.^[67] proposed the adsorption of a Li-S^{*} radical (representing lithium polysulfide species^[68] for simplicity) on the given crystalline surfaces of oxides (i.e., MgO(100) and ZnO(0001)) (see Figure 8(e, f)). According to the DFT calculations, it is found that the binding energy (5.40 eV) of the sulfide species to ZnO was considerably larger than that (1.22 eV) to MgO. Thus, Yu et al.^[67] concluded that the excellent electrochemical performance of ZnO/G-S might be due to the dual protection effects from the ALD coating and the porous graphene architecture: (i) the ALD coatings acted as kinetic barriers to reduce the direct contact between active sulfur species and the liquid electrolyte, thereby improving the mechanical/structural stability of electrodes over prolonged cycling, and (ii) the porous graphene architecture formed the quasi-envelop structure of G-S and therefore weakened the release of polysulfides from the electrode to the electrolyte. SEM observation also verified that there were irreversible deposition and aggregation of insoluble reduction products (i.e., Li₂S/Li₂S₂) on the bare G-S cathode, while the amount of insoluble lithium sulfides on the two ALD-coated cathodes were comparatively less pronounced after 100 discharge-charge cycles.

Yu et al. also investigated the effects of ALD-TiO₂ on sulfur composite cathodes.^[69] In the study, Yu et al. utilized nitrogen-doped graphene (NG) as a carbon matrix for sulfur impregnation (see Figure 9(a)). The mixture of NG and sublimed sulfur was treated by ball milling for 2 h, and then heated at 155 °C for 12 h. The obtained NG/S composite was further mixed with carbon black and polyvinylidene difluoride binder with a mass

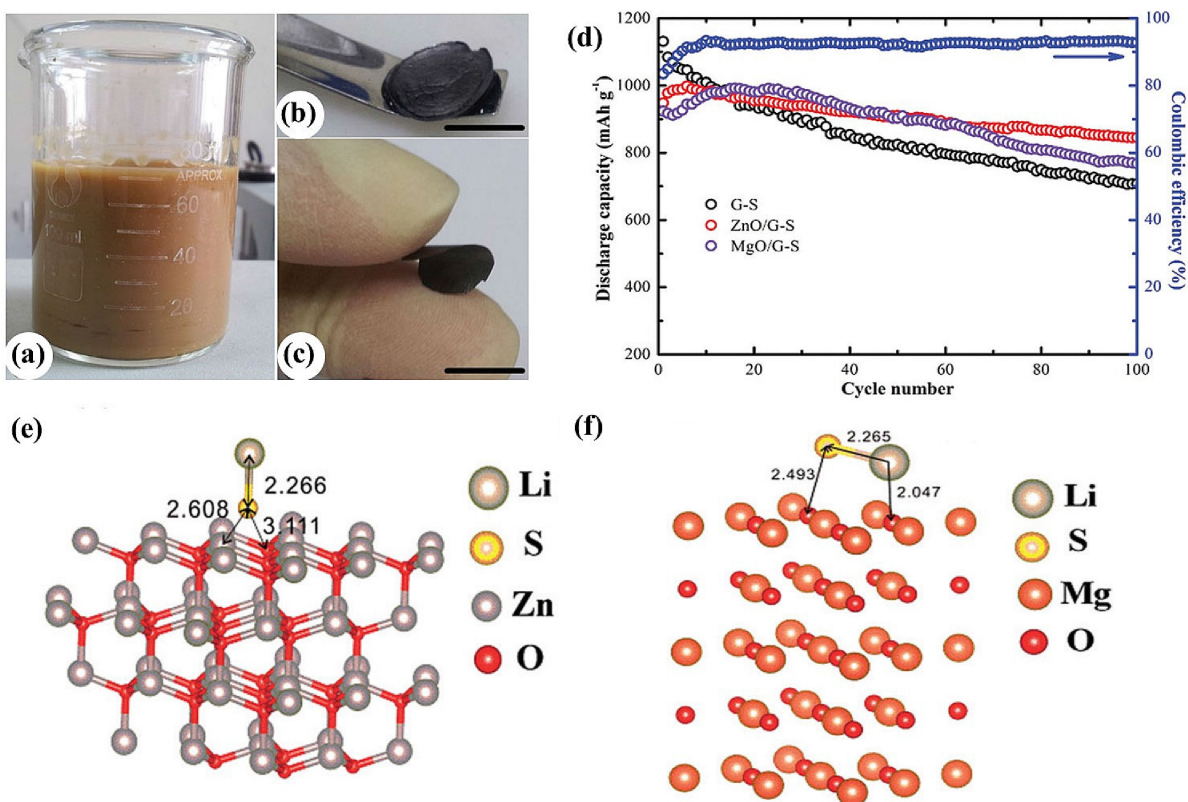


Figure 8. Digital images of (a) GO–S dispersion, (b) as-obtained G–S hydrogel, and (c) a bent-G–S aerogel. (d) Cycling performance of the composite electrodes at a rate of 0.2 C. (e,f) DFT simulations show the most stable configurations and calculated binding energies of Li–S[•] with ZnO and MgO.^[67] Reprinted (adapted) with permission from ref. 67. Copyright (2015) Royal Society of Chemistry.

ratio of 8:1:1 for fabricating S-NG cathodes. The ALD-TiO₂ was performed on the fabricated NG/S electrodes using titanium tetraisopropoxide (TTIP) and H₂O as precursors at 150 °C. The cathodes were denoted as NG/S and NG/S-xTiO₂ ($x = \text{ALD}$ cycles). Electrochemical characterization based on CV profiles disclosed that NG/S-20TiO₂ had two peaks at 2.0 and 2.3 V during cathodic scanning, and two peaks at 2.3 and 2.4 V during anodic scanning in ten cycles. Interestingly, the CV curves did not change considerably with NG/S-xTiO₂ ($x = 0, 5, 10, 40$), indicating TiO₂ coatings have little influence on the Li–S redox reaction mechanism. In particular, comparing the CV curves of the NG/S electrodes with and without TiO₂ coatings, Yu et al.^[69] discovered that the ALD-TiO₂ coatings rendered the onset potentials of the two cathodic curves shifted positively while those of the anodic curves shifted negatively, i.e., the ALD coatings narrowed the potential separation of redox curves. This implies that the ALD coatings have improved the electrochemical kinetics of the electrode reactions. Rate capability measurements revealed that, along with the increase of current density from 0.1 to 4 C, the ALD coated electrodes always showed better rate capacities. It was believed that the bare NG/S composite cathode has suffered from serious dissolution of polysulfides. Among all the coated and uncoated cathodes, NG/S-20TiO₂ performed the best, starting from a capacity of 1102 mAh/g and ending with a capacity of 918.3 mAh/g after 500 electrochemical cycles. This finding further suggested that the shuttling behaviors of polysulfides

have been greatly reduced, which was ascribed to the microstructure of NG being able to improve lithium ion diffusion, and the optimal thickness of ALD-TiO₂ coating resulting in the formation of kinetic barrier. In addition, the hydrophilic TiO₂ might have also produced favorable interactions with polysulfides to bind them on the cathode.

To gain an insight on the experimental findings, Yu et al.^[69] conducted DFT calculations to study the interaction between polysulfides and TiO₂. In the simulation, the crystalline phases of TiO₂ (i.e., anatase-TiO₂ (101) and rutile-TiO₂ (110)) were applied, since they have the most stable structures with the lowest surface energy.^[70] The DFT results^[69–70] showed that the binding energy of sulfur-containing species (radical Li–S[•] representing lithium polysulfide species^[71] for simplicity) was ~2.30 eV to anatase-TiO₂ (101) (see Figure 9(b)), while 2.18 eV to rutile-TiO₂ (110) (see Figure 9(c)). The binding energy of the final discharge product Li₂S to anatase-TiO₂ (101) and rutile-TiO₂ (110) were 3.59 and 3.62 eV (see Figure 9(d,e)), respectively. The increased binding energies imply that the chemical binding strength mainly comes from the lithium ions. In particular, compared with the adsorption binding energies of Li–S composites on graphene (<1 eV),^[72] these values are much larger, indicating that TiO₂ have played an important role in trapping polysulfide anions.

Recently, a study used ALD V₂O₅ coatings on sulfur-filled carbon nanotubes (CNTs).^[73] In the work, Carter et al.^[73] deposited various cycles of V₂O₅ coating using the precursors of

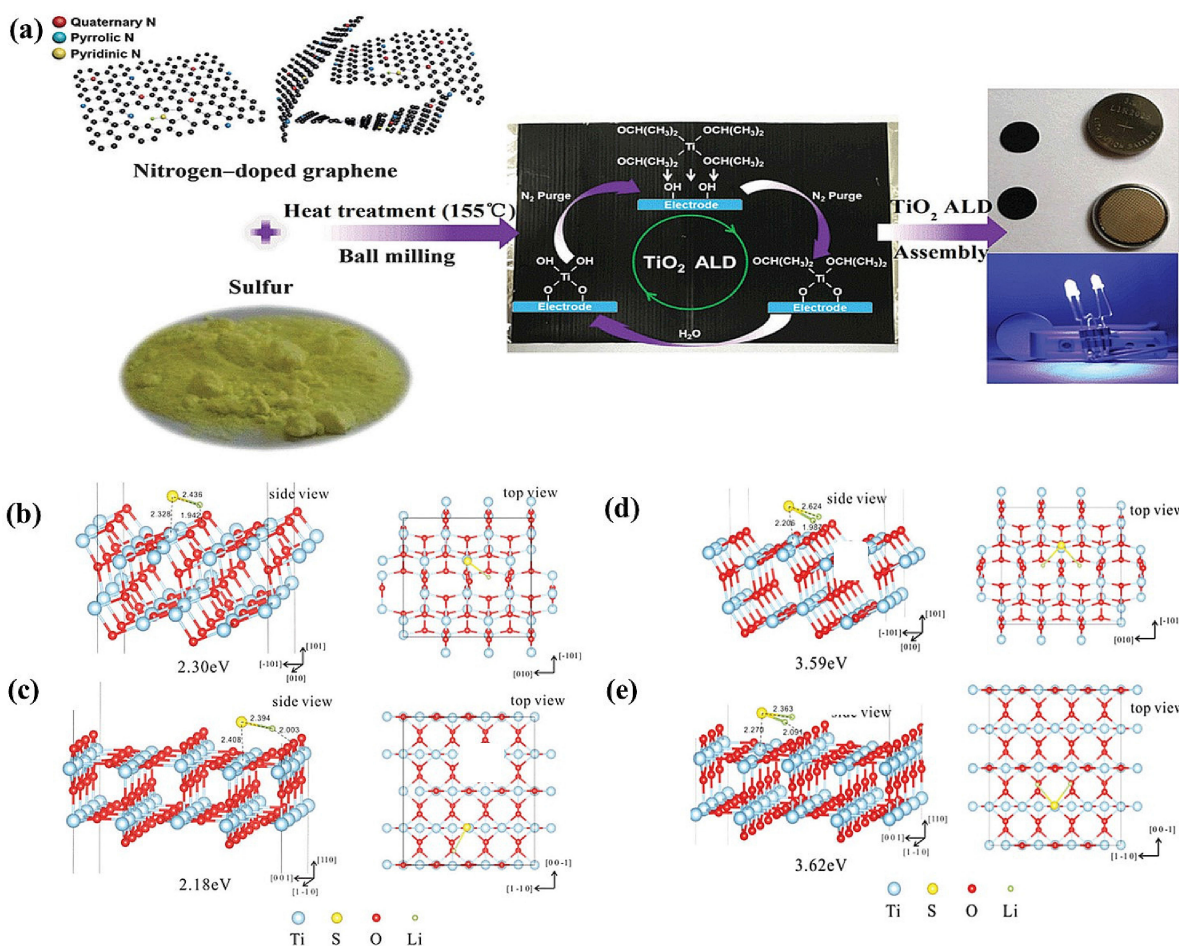


Figure 9. (a) Preparation process of NG/S-TiO₂ and their cell performance. DFT simulations on the adsorption configuration of Li-S* on (b) the anatase TiO₂(101) surface and (c) the rutile TiO₂(110) surface. DFT simulations on the adsorption configuration of Li₂S on (d) the anatase TiO₂(101) surface and (e) the rutile TiO₂(110) surface.^[69] Reprinted (adapted) with permission from ref. 69. Copyright (2016) Royal Society of Chemistry.

VO(OC₃H₇)₃ and H₂O at 150 °C. The V₂O₅ coatings are 3.7, 5.5 and 7.4 nm for 50, 75 and 100 ALD cycles, respectively. The infiltrated sulfur in CNTs has a loading of 65 wt%. Using the ALD V₂O₅ coatings and the CNT confinements, Carter et al.^[73] made an effort to accomplish the best performance of Li–S batteries (see Figure 10(a)). Among all the samples, Carter et al. found that the 75-cycle (5.5 nm) ALD-V₂O₅ coated S-filled CNTs exhibited the best electrochemical behaviors, in terms of sustainable capacity and CE. Electrochemical measurements at 0.1 C (see Figure 10(b)) disclosed that the uncoated CNTs exhibited a capacity of 945 mAh/g initially but faded to 600 mAh/g only after 25 cycles. In comparison, both 50- and 75-cycle ALD V₂O₅ coated S-filled CNTs showed higher initial capacity (1043 and 1209 mAh/g, respectively) than that of the pristine S-filled CNT cathode, while the 100-cycle ALD V₂O₅ coated S-filled CNTs exhibited an initial capacity of 826 mAh/g. Further investigation was conducted for 75-cycles ALD-V₂O₅ at 0.2 C, the V₂O₅ coated S-filled CNT cathode started from an initial discharge capacity of 800 mAh/g and remained 87% and 73% of the initial capacity after 100 and 450 cycles, respectively (see Figure 10(c)). Carter et al.^[73] believed that the exterior V₂O₅ layer coated on the CNT surfaces might have helped anchor

lithium polysulfides while the CNTs also might have helped confine polysulfides from shuttling. In comparison, the 50-cycle and 100-cycle V₂O₅ were inferior to the 75-cycle V₂O₅ layer. The 50-cycle V₂O₅ layer might not be as effective as the 75-cycle V₂O₅ layer while the 100-cycle ALD-V₂O₅ coating might have impeded the charge transfer at the electrode interface, due to the formation of a thick conformal film of V₂O₅.

In summary, all the ALD coatings (i.e., Al₂O₃, ZnO, MgO, TiO₂, and V₂O₅) have demonstrated their effectiveness in inhibiting the shuttle behaviors of polysulfides, and their roles could lie in two aspects, i.e., adsorbents of sulfur-containing species and/or kinetic barriers. To get a clearer picture on their roles in determining the Li–S battery performance, these ALD coatings and their effects have been summarized in Table 1. To further elucidate the trends of these ALD coatings, systematic studies based on extensive DFT calculations can be insightful for the screening of electronic properties and energy absorption of the radical Li–S* on various bare and hydroxylated metal oxide surfaces.

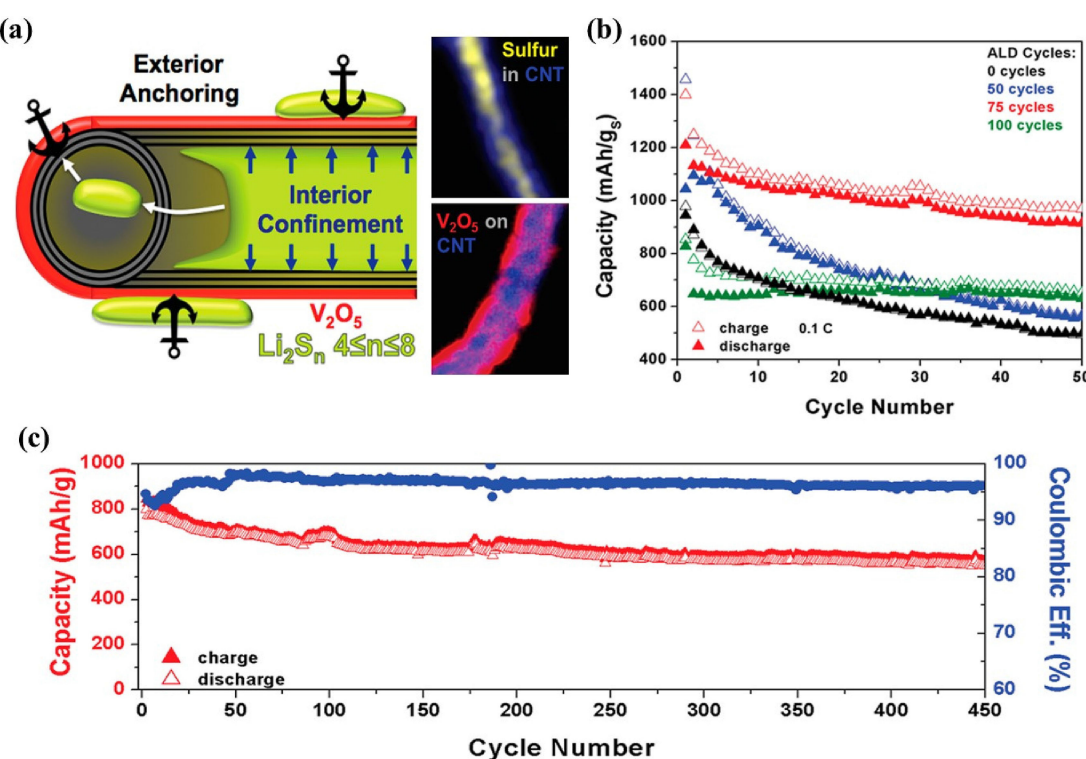


Figure 10. (a) Schematic of sulfur loaded on CNT to achieve excellent conversion via interior confinement and exterior V_2O_5 anchoring layer to lithium polysulfide. (b) The effect of ALD coating thickness on sustainable capacity at 0.1 C. (c) A long cycling test at 0.2 C was performed on the electrode coated with 75 ALD cycles of V_2O_5 , achieving ~73 % capacity retention after 450 cycles.^[73] Reprinted (adapted) with permission from ref. 73. Copyright (2017) American Chemical Society.

Table 1. ALD coatings on S/Li₂S cathodes.

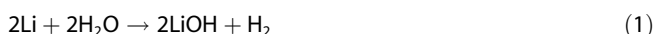
ALD coat- ings	S/Li ₂ S catho- des	ALD parameters	Electrolytes	Roles of coatings	Ref.
Al_2O_3	S-ACF	170 °C, TMA + O ₂ plasma, < 5 nm	3 M LiTFSI in 1:1 DIOX/DME with 0.2 M LiNO ₃		[63]
	G-S	120 °C, TMA + H ₂ O, 5 or 10 cycles	1 M LiTFSI in 1:1 DOL/DME		[6]
	S nanopar- ticles	50 °C, TMA + H ₂ O, 0.5–11 nm	1 M LiTFSI in 1:1 DOL/DME		[64]
	Li ₂ S-GS	120 °C, TMA + O ₃ , 0.55–3 nm	1 M LiTFSI in 1:1 DOL/DME with 1 wt% LiNO ₃		[65]
	CMWF	150 °C, TMA + H ₂ O, 5 nm	1 M LiTFSI in 1:1 DOL/DME with 1 wt% LiNO ₃		[66]
ZnO	¹ ACC	150 °C, TMA + H ₂ O, 0.5 nm	1 M LiTFSI in TEGDME	(i). Reducing lithium polysulfide dissolution; (ii). Suppressing S shuttling behaviors; (iii). Enhancing the cycle stability; (iv). Improving the integrity of the electrode; (v). Serving as chemical adsorbents and physical barrier to polysulfides.	[90]
		120 °C, DEZ + H ₂ O, 40 cycles			
MgO	G-S	120 °C, Mg(CpEt) ₂ + H ₂ O, 40 cycles	1 M LiTFSI in 1:1 DOL/DME		[67]
TiO_2	NG/S	150 °C, TTIP + H ₂ O, 2–4 nm	1 M LiTFSI in 1:1 DOL/DME with 2 wt% LiNO ₃		[69]
	N-doped car- bon	250 °C, TiCl ₄ + H ₂ O, 0.34 nm	1 M LiPF ₆ in 1:1 ² FEC/EMC; 0.325 M LiTFSI in 1:1 DOL/DME with 0.675 M LiNO ₃		[53]
V_2O_5	CNT	150 °C, $VO(OC_3H_7)_3$ + H ₂ O, 3.7, 5.5, and 7.4 nm	1 mM Li ₂ S ₆ in 1:1 DOL:DME with 0.25 M LiNO ₃		[73]

Note: 1. Reactivation interlayer. 2. FEC/EMC = Fluoroethylene carbonate/ethyl methyl carbonate.

3.1.2. Lithium Metal Anodes

As an alternative to LIBs, Li–S batteries enable a much higher theoretical energy density up to 2600 Wh/kg, in which lithium metal is used as the anode with a high theoretical capacity of 3860 mAh/g and the lowest electrochemical potential –3.04 V versus SHE (standard hydrogen electrode).^[24a,25b,74] These attractive merits make lithium metal an ideal anode material for high-energy rechargeable lithium batteries. However, the lithium metal anode to date has been hindered from commercialization by many technical issues, such as the lithium dendrite growth during repeated lithium extraction and deposition processes, the interfacial instability between the lithium metal and an electrolyte, and the metallic lithium corrosion during the operating condition of Li–S batteries. In addition, the combustible gas generation during the formation of SEI poses another serious issue related to the safety of Li–S batteries. As a result, there have been many technical strategies investigated for addressing the issues faced by lithium metal anodes, such as passivating the lithium anode with polymer films,^[75] solid electrolytes,^[76] chemical additives,^[77] and surface coatings.^[78]

Among these strategies, there have been ALD coatings reported for tackling the issues associated with lithium metal anodes in Li–S batteries. Aimed at alleviating in the corrosion of lithium metal, Kozen et al.^[79] made the first attempt using ALD to deposit ultrathin Al₂O₃ coatings over Li metal anodes with the precursors of TMA and O₂ plasma at 150 °C. By coating the lithium metal foils with 5- and 14-nm of ALD-Al₂O₃, respectively, Kozen et al.^[79] studied the effects of ALD coatings under different Li–S operating conditions. Based on XPS measurements, the characteristic peaks of both Li and Al₂O₃ were found on the 5-nm Al₂O₃ coated Li metal sample, whereas on the 14-nm Al₂O₃ coated Li metal sample, the Li 1s peak associated with the pristine Li metal was not observed. This implies that the 14-nm ALD coating has formed a uniform and conformal protecting film over the Li metal surface. Exposed in air, it was found that the pristine Li metal was tarnished within 1 min whereas the 14-nm ALD-Al₂O₃ protected sample survived for ~20 hours. To test the stability against organic solvent electrolyte, both the pristine and ALD-coated lithium metal samples were immersed in the propylene carbonate (PC) solution, and the corrosion and reaction was studied using mass spectroscopy. For a bare lithium metal, the possible oxidation reactions are described in Equations (1) and (2):



Thus, the H₂ release can serve as the indicator of corrosion reaction. In the study,^[79] Kozen et al. revealed that the H₂ partial pressure of the bare lithium metal sample was much higher than that of the Al₂O₃ protected Li metal sample (see Figure 11(a)), suggesting that the ALD coatings have considerably mitigated the degradation of lithium metal. Kozen et al.^[79] found that the ALD coatings of <15 nm exhibited a self-healing mechanism, i.e., a stable phase could be formed at some defect

sites in the ALD coatings by local electrolyte decomposition reactions and then the corrosion reaction was diminished. By correlating the onset time of the atmospheric tarnishing and the onset time of the H₂ evolution with ALD coating thickness from the samples (see Figure 11(b)), Kozen et al.^[79] disclosed that an effective thickness dependence of the ALD Al₂O₃ coatings was ~1.8 h/nm for both the atmospheric and solvent exposure. Furthermore, Kozen et al.^[79] performed another corrosion testing by immersing lithium metal samples into a solution with elemental sulfur and dimethoxyane (DME). The experiments indicated that the 14-nm ALD-Al₂O₃ coated Li metal outperformed the bare Li metal anode, in terms of chemical stability for (Figure 11(c) unprotected and for (Figure 11(d) 14 nm ALD Al₂O₃-protected Li metal foil after both samples being soaked in 1 M sulfur/DME solution for seven days. CV measurements (see Figure 11 (e, f)) further showed that the protected Li metal exhibited two different slopes corresponding to two different domains for Li plating (see Figure 11(e)), which might be attributed to the changing of interface impedance during the lithiation process of the Al₂O₃ coating film. In contrast, the current of the bare Li metal was linearly proportional to the electrode potential throughout the first three CV cycles (see Figure 11(f)). In the case of the protected Li metal sample, a non-uniform plating and stripping process related to the ALD coating was observed in the first three cycles (Figure 11(e)) before eventually going into saturation similar to the bare sample after three CV cycles (see Figure 11(e) insert). Kozen et al.^[79] further investigated the effectiveness of the ALD-coated Li metal anodes in Li–S batteries, in which a carbon-supported S cathode (i.e., S deposited on activated carbon cloth) was adopted. They disclosed that the cell with a bare Li metal anode exhibited an initial discharge capacity of 1200 mAh/g, but then dropped to 800 mAh/g after the first 10 cycles, and 600 mAh/g after 100 cycles. In contrast, the Li–S cell with a 14 nm ALD-Al₂O₃ coated Li anode showed a high discharge capacity of 1200 mAh/g initially and could maintain 90 % of the initial capacity after 100 cycles with a CE of >95 %. This clearly demonstrated that the ALD-Al₂O₃ coated Li anode could significantly prevent the Li–S cells from self-discharge^[80] and capacity fading, and therefore greatly boost the Li–S cells' electrochemical performance.

In addition to Kozen et al.,^[79] Kazyak et al.^[81] also investigated the roles of ALD-Al₂O₃ coatings on Li metal anodes. Using symmetric cells (i.e., two identical electrodes separated by a separator in an electrolyte), Kazyak et al.^[81] reported that, using ALD, the 2–3 nm Al₂O₃-coated Li electrodes survived a much longer cycling lifetime than the bare Li electrodes. Kazyak et al.^[81] further observed that, among the ALD-Al₂O₃ coatings, the 20-cycle ALD-Al₂O₃ coated anode resulted in the longest cell cycling lifetime among the 10-, 20-, 30-, 40-, and 100-cycle ALD coated ones. In terms of the electrochemical cycling profiles (see Figure 12(a)), all the cells showed a decrease in their overpotentials at the very beginning possibly due to the SEI formation, then stabilized to lower overpotentials after 10-h cycling (i.e., 0.12 V for the control cell, 0.08 V for the 20-cycle ALD Al₂O₃ cell, and 0.11 V for the 30-cycle Al₂O₃ cell). The cells' overpotentials increased sharply once a failure occurred to

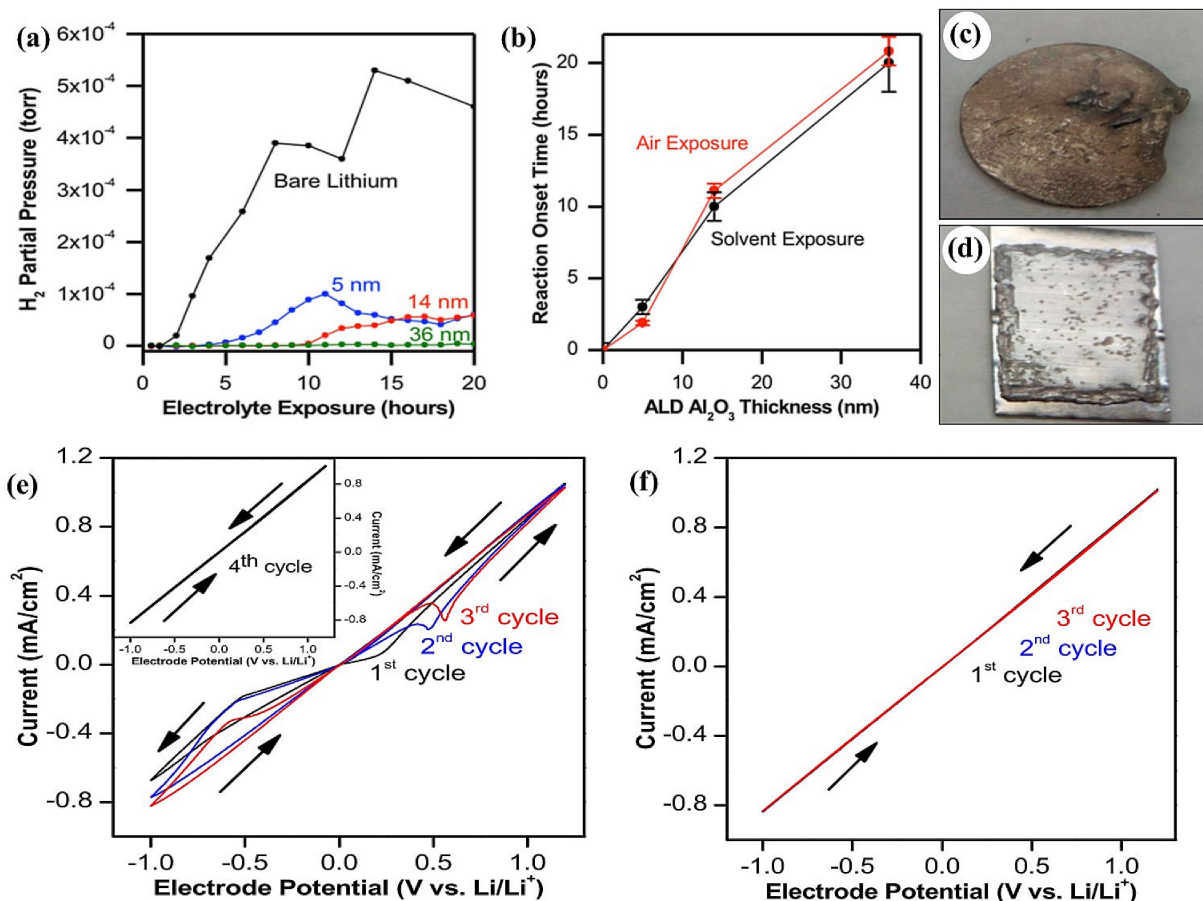


Figure 11. (a) Evolution of H_2 during organic solvent exposure. (b) Correlation between onset time for atmospheric tarnishing and onset time for H_2 evolution. Optical images of (c) bare Li metal and (d) protected Li metal. (e) The plots of the first three CV cycles of a lithium metal anode protected with 14 nm ALD Al_2O_3 (inset: the fourth CV cycle). (f) The plots of the first three cycles of a bare lithium metal anode.^[79] Reprinted (adapted) with permission from ref. 79. Copyright (2015) American Chemical Society.

them, such as 0.61 V for the control cell and 0.62 V for the 30-cycle ALD-Al₂O₃ cell. This rapid increase in overpotential was due to the electrolyte decomposition. In comparison, the 20-cycle ALD-Al₂O₃ cell could remain stable voltage behavior for longer cycles. The changes in cell overpotentials were also consistent to the impedance measurements (see insets of Figure 12(a)). Obviously, the cell impedance of the ALD-Al₂O₃ coated electrodes (e.g., the 20-cycle coated electrodes) exhibited much smaller impedance throughout different cycling stages. This implies that the ALD coated anode could greatly improve the interfacial stability against the undesirable parasitic reactions between the Li metal and the electrolyte. This finding is also consistent to the observation reported by Kozen et al.^[79]. In order to further understand the structural evolution, SEM was employed to characterize the morphological changes of the control electrode and the 20-cycle ALD-coated Li electrodes (see Figure 12(b–e)). After the first 100 electrochemical cycles, the control electrode (see Figure 12(b)) exhibited a rough, porous and textured surface, while the 20-cycle ALD-coated Li electrode (see Figure 12(c)) showed a smooth and dense morphology. After the cell failure, a much more rough and porous surface could be discovered for the control electrode (see Figure 12(d)), however, the ALD-coated electrode displayed

an extreme dense morphology with infrequent localized dendrites (see Figure 12(e)). These results strongly suggested that the ALD coatings evidently inhibited the Li dendrite growth, and therefore ALD is capable of mitigating the electrolyte decomposition, and subsequently extends the Li–S cell lifetime.

The protective roles of the ALD-Al₂O₃ coatings recently further prompted another insightful study conducted by Lin et al.^[82] Using SEM and EDX mapping, Lin et al. confirmed that SEI was more prone to form preferentially on boundaries and ridges of Li metal surface (see Figure 13(a)). By applying ALD-Al₂O₃ coatings on Li metal, Lin et al. showed that there had no remarkable morphological change for the ALD coated Li-metal when immersed in PC solvent solution, according to in-situ AFM (atomic force microscopy) characterization, except for some continuous increases in surface roughness at some scratched areas (see Figure 13(b)). This evidence further suggested that the ALD coatings could play a critical role in protecting Li metal from undesirable reactions with the carbonate-based solvent. In comparison with the bare Li metal, the ALD-coated Li metal had a much slower growth rate in surface roughness (see Figure 13(c)), accounting for $0.15 \pm 0.18 \text{ nm/h}$ versus $2.01 \pm 0.26 \text{ nm/h}$ for the bare Li metal. Besides

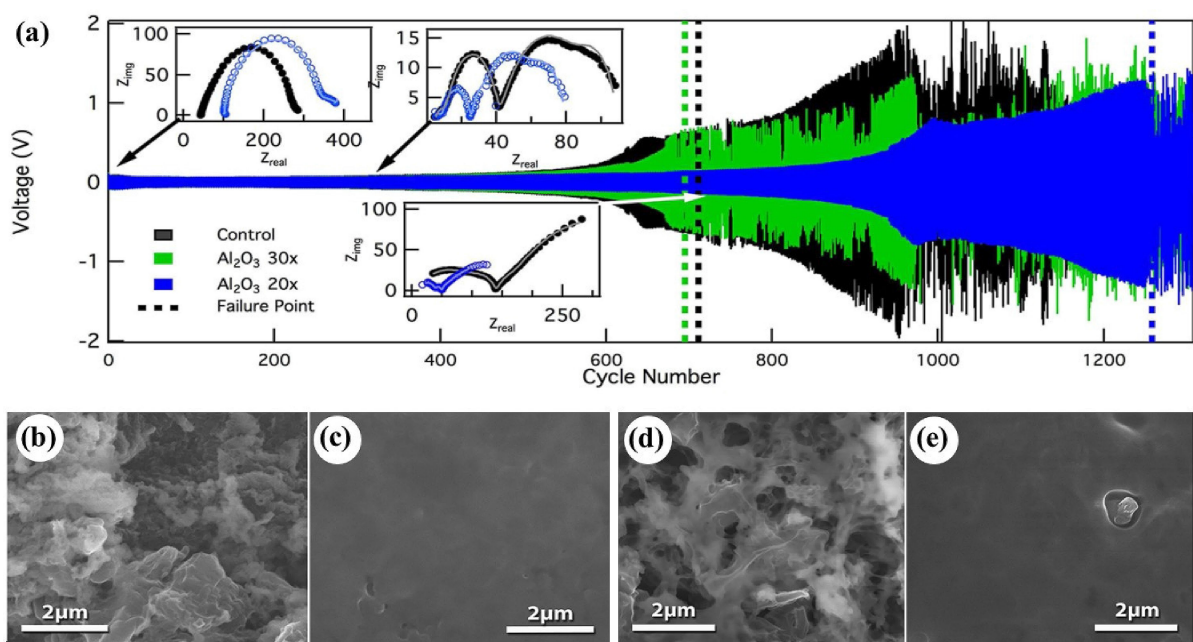


Figure 12. (a) Voltage profiles of Li symmetric cells, showing the effects of ALD coatings on overpotential evolutions at 1 mA/cm^2 for 0.25 mAh/cm^2 . In the plots, the dotted lines represent the point of failure for each cell. EIS measurements were taken after 0, 300, and 700 cycles, as shown in insets. SEM images of morphological changes for (b, d) the control Li electrode and (c, e) the 20-cycle Al₂O₃ coated Li electrode.^[81] Images were taken after (b,c) 100 cycling times and (d, e) failure (ca. 1280 cycles). Reprinted (adapted) with permission from ref. 81. Copyright (2015) American Chemical Society.

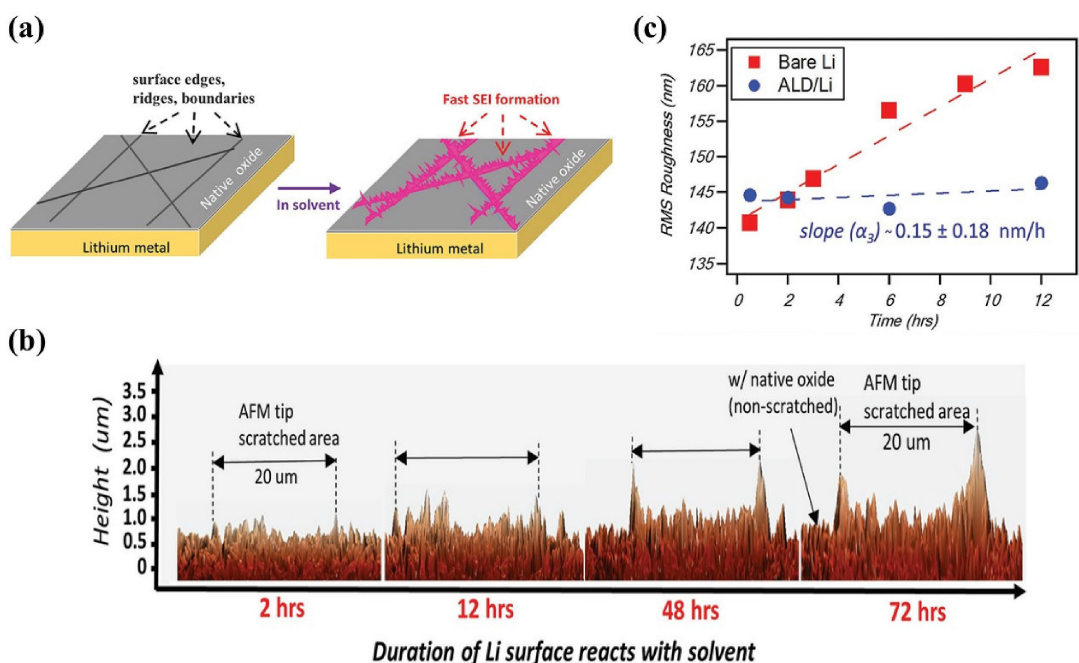


Figure 13. (a) Schematic illustration on the fast SEI growth at surface microstructures. (b) 3D cross-sectional EC-AFM images show the evolution of the height morphology at various duration time of Li surface solvent reaction. (c) Average RMS roughness of a $20 \mu\text{m} \times 20 \mu\text{m}$ scanned area on an ALD coated Li (blue) and a bare Li (red).^[82] Reprinted (adapted) with permission from ref. 82. Copyright (2016) John Wiley and Sons.

the PC solvent, the bare and coated Li metal have also been examined in other solvents, i.e., 1:1 DME/DOL and dimethyl sulfoxide that widely used in Li–S batteries. In 1:1 DME/DOL solution, the H₂ gas was released and detected only with the bare Li metal sample, which indicated that the ALD coatings

were effective in suppressing the unwanted parasitic reactions. For symmetric cells using the electrolyte of 1 M LiPF₆ in 1:1 ethylene carbonate (EC)/dimethyl carbonate (DEC), Lin et al.^[82] found that the Li–S cell with the bare Li electrodes produced much higher H₂ partial pressure, whereas the Li–S cell with the

ALD-coated Li anode was electrochemically stable without releasing noticeable H₂. This further confirmed that an ultrathin ALD-Al₂O₃ film could dramatically improve the cycling lifetime of the Li electrodes by avoiding the electrolyte degradation.

More recently, Chen et al.^[83] deposited 10 and 20 ALD cycles of Al₂O₃ on lithium metal anodes (i.e. 10×Al₂O₃ Li and 20×Al₂O₃ Li, respectively) at 150 °C using TMA and water as precursors. The ALD coated Li anodes were then examined in carbonate-based (1.0 M LiPF₆ in EC/EMC, 3:7 v/v) and ether-based (1.0 M LiTFSI + 0.18 M Li₂S₈ + 2 wt% LiNO₃ in DOL/DME, 1:1 v/v) electrolytes. Chen et al.^[83] disclosed that the ALD Al₂O₃ coatings improved the wettability of Li metal anodes to the two electrolytes (see Figure 14(a)). Using the carbonate electrolyte, isolated droplets were formed on the bare Li electrode, while there were no visible droplets on the 10× and 20×Al₂O₃ protected Li anodes. A similar phenomenon has also been observed with the ether electrolyte. Chen et al.^[83] believed that an improvement in the wettability of Li anodes could help lead to a more uniform lithium ion transport, enable more uniform Li electrodeposition, and subsequently enhance the CE of the Li–S cell. In addition, the morphologies of the bare Li (see Figure 14(b)) and 20×Al₂O₃ Li (see Figure 14(c)) anode were observed using SEM after 50 charge-discharge cycles in symmetric cells. The bare Li anode surface was covered by a layer of thick SEI films and dendrites, which would accelerate the electrolytes degradation, and even shut-off a working anode with escalated impedances. In comparison, the 20×ALD-Al₂O₃ Li anode maintained a smooth, uniform surface morphology due to the excellent electrolytes wettability on the surface.^[84] In order to help explain the roles of Al₂O₃ on Li metal

anodes, Chen et al.^[83] established a model (see Figure 14 (d1,2)). Chen et al.^[83] believed that, as shown in Figure 14(d1), the poor wettability of electrolytes on the bare Li metal resulted in a non-uniform electrolytes/anode interface. This might have led to the formation of inhomogeneous dendritic structures. In contrast, the uniform Al₂O₃ coating on the Li metal anode (Figure 14(d2)) provided a uniform electrolytes/anode interface and surface wettability, and therefore enabled a uniform Li stripping and plating due to relatively more uniform Li⁺ transport through the interface. During lithiation and delithiation process in the charge/discharge of the cell, the assumed uniform Li⁺ transport can be facilitated by Li⁺ diffusion through the ALD Al₂O₃ layer at the vicinity of the Li metal surface.^[83] During cell charges, the lithiation process might possibly have led to the formation of a LiAlO₂ layer, having an ionic conductivity ~6×10⁻⁸ S/cm at room temperature,^[85] which is much higher than the calculated conductivity of Li in amorphous Al₂O₃ (5×10⁻¹⁰ S/cm⁻¹) at room temperature.^[86] Chen et al.^[83] further investigated the effects of the ALD Al₂O₃ films on electrolyte volume and cycling life in symmetric cells. Chen et al.^[83] found that, for the bare Li cell, the electrolyte depleted rapidly due to the continuous SEI formation, leading to a significantly increased cell impedance and voltage. The battery failure occurred after 140 hours. In contrast, the ALD protected Li anode yielded a more stable voltage profile. The 20×Al₂O₃ Li electrode maintained a constant voltage of 100 mV after 100 hours.

In comparison to the efforts on ALD-Al₂O₃ coatings discussed above, a recent study^[87] on a solid-state electrolyte of Li_xAl_yS is more significant, featuring a much better ionic

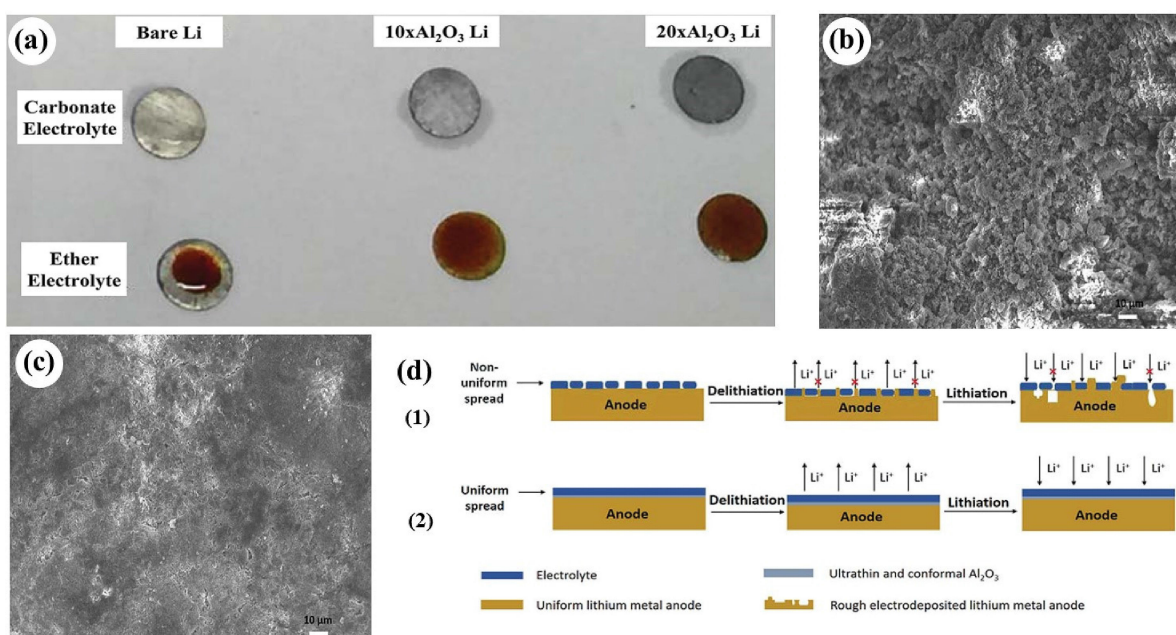


Figure 14. (a) Photographs of electrolyte wettability on bare Li (left), 10×Al₂O₃ coated Li (middle), and 20×Al₂O₃ coated Li (right), using carbonate (top) and ether (bottom)-based electrolytes. SEM images of Li metal surfaces after 50 charge-discharge cycles in symmetric cells at the current density of 1 mA/cm² and capacity of 1 mAh/cm² for (b) bare Li and (c) 20×Al₂O₃ coated Li. (d) Schematic illustration of lithium electrodeposition on lithium metal anode via electrolyte: (1) rough lithium electrodeposition through poorly wetted, bare lithium surface and (2) uniform and smooth lithium electrodeposition through uniformly wetted, ALD Al₂O₃ coated lithium surface.^[83] Reprinted (adapted) with permission from ref. 83. Copyright (2017) Royal Society of Chemistry.

conductivity over Al_2O_3 . Using ALD, Cao et al.^[87] deposited a $\text{Li}_x\text{Al}_y\text{S}$ compound at 150 °C on Li metal anodes and Cu foils by combining two individual sub-ALD processes of $\text{Li-S}^{[88]}$ and $\text{Al-S}^{[89]}$ in a cycle ratio of 1:1. In Li/Li symmetric cells (using the electrolyte of 1 M LiPF_6 in 3:7 EC/EMC), electrochemical impedance spectroscopy (EIS) was used to investigate the interfacial stability of Li metal electrodes (see Figure 15(a,b)). Cao et al.^[87] revealed that the interface between the $\text{Li}_x\text{Al}_y\text{S}$ -coated Li metal and the electrolyte was much more stable than the uncoated pristine Li metal/electrolyte interface, showing a much smaller and more stable resistance across the SEI layer (see Figure 15(a,b)). This is consistent with the observations made by Kazyak et al.^[81] and Lin et al.^[82]. Using asymmetric cells consisting of a Li metal and Cu foil, Cao et al.^[87] disclosed that the cell with a $\text{Li}_x\text{Al}_y\text{S}$ -coated Cu foil exhibited a much higher CE and a longer cycling life than the one with a bare Cu foil. This implies that the $\text{Li}_x\text{Al}_y\text{S}$ coating on the Cu foil could protect and stabilize the lithium metal effectively. According to their findings, the cells with the bare Cu foil exhibited a decreasing CE from 80% to 40% in 150 cycles, while the cell with the $\text{Li}_x\text{Al}_y\text{S}$ -coated Cu maintained a stable CE (80%) even after 170 cycles. SEM observation (see Figure 15(c-f)) further revealed that, after the 1st lithium deposition, there were numerous needle-like Li dendritic structures formed on the bare Cu foil (see Figure 15 (c,e)) while there were no dendrite-like structures found on the $\text{Li}_x\text{Al}_y\text{S}$ -coated Cu foil (see Figure 15 (d,f)). Thus, the $\text{Li}_x\text{Al}_y\text{S}$ coating has helped effectively reduce the parasitic reaction

between Li metal and electrolyte and enhanced the cell stability significantly^[87]. In particular, the ionic conductivity was measured being as high as 2.5×10^{-7} S/cm at room temperature for the ALD $\text{Li}_x\text{Al}_y\text{S}$ coating. In this regard, the ALD $\text{Li}_x\text{Al}_y\text{S}$ coating could be much better than the ALD Al_2O_3 coating, and provided a new route for tackling the problematic issues related to Li dendrite growth.

In short, both the ALD coatings of Al_2O_3 and $\text{Li}_x\text{Al}_y\text{S}$ were discovered to be conducive and could improve the stability of the interface between the Li metal and electrolyte by reducing the unwanted electrolyte consumption and Li metal corrosion, and subsequently suppress the uncontrolled growth of dendrite formation. The various benefits and the improvement of Li-S battery performance attributed to the Al_2O_3 and $\text{Li}_x\text{Al}_y\text{S}$ coatings at Li metal anode are summarized in Table 2.

3.1.3. Reactivation Layer by ALD

In addition to the efforts using ALD coatings on lithium metal anodes and S/Li₂S cathodes, there was also an attempt^[90] in modifying separators for achieving high-performance Li-S batteries. In the work, Han et al. conducted the deposition of ALD Al_2O_3 at 150 °C on activated carbon cloth (ACC) with the precursors of TMA and water. Coated with 0.5 nm thick Al_2O_3 , the resultant ACC was assembled into a Li-S cell as a reactivation layer, locating between the S cathode and the

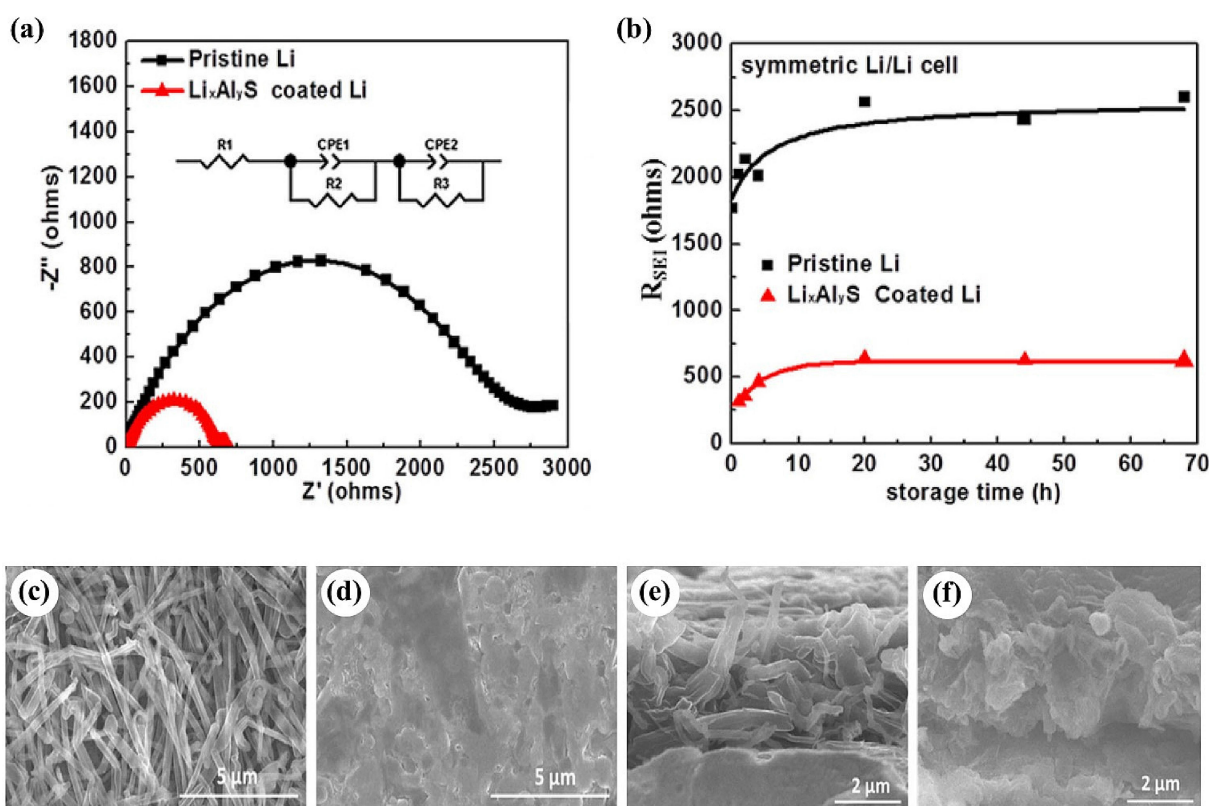


Figure 15. (a) AC impedance spectra of Li/electrolyte/Li symmetric cells using both pristine Li and $\text{Li}_x\text{Al}_y\text{S}$ -coated Li after 68 h storage. (b) R_{SEI} of Li/electrolyte/Li symmetric cells versus storage time. (c,d) Top-view and (e,f) cross-sectional SEM images of Li metal deposited on (c,e) pristine Cu and (d,f) Cu coated with 50 nm $\text{Li}_x\text{Al}_y\text{S}$ ALD film.^[87] Reprinted (adapted) with permission from ref. 87. Copyright (2016) John Wiley and Sons.

Table 2. ALD coatings on Li metal via ALD.

ALD coatings	ALD parameters	Electrolytes	Roles of coatings	Ref.
Al_2O_3	150 °C, TMA + O ₂ plasma, 5 nm, 14 nm	0.1 M LiTFSI in 1:1 DOL/DME + 1% LiNO ₃		[79]
	100 °C, TMA + H ₂ O, 2–3 nm (20 ALD cycles), 3–4 nm (30 ALD cycles)	1 M LiPF ₆ in 1:1 EC/ DMC	(i). Stabilizing the Li/electrolyte interface; (ii). Suppressing Li degradation; (iii). Eliminating electrolyte decomposition;	[81]
	100 °C, TMA + O ₂ plasma, 10.5 nm	1 M LiPF ₆ in 1:1 EC/ DEC	(iv). Improving mechanical integrity;	[82]
	150 °C, TMA + H ₂ O 4 nm	1 M LiPF ₆ in 1:1 EC/ EMC	(v). Preventing Li dendrite growth.	[93]
	150 °C, TMA + H ₂ O, 2.5 nm, 4 nm	1.0 M LiPF ₆ in 3:7 EC/ EMC 1.0 M LiTFSI + 0.18 M Li ₂ S ₈ + 2 wt% LiNO ₃ in 1:1 DOL/DME		[83]
$\text{Li}_x\text{Al}_y\text{S}$	150 °C, Li ₂ S: LTB + H ₂ S, Al ₂ S ₃ :TDMA- Al + H ₂ S, 50 nm	1 M LiPF ₆ in 3:7 EC/EMC	Increasing capacity, CE and lifetime; Improving the ionic conductivity.	[87]

separator. In comparison to the bare ACC, the Al_2O_3 -coated ACC was more favorable to reactivate lithium polysulfides. Ascribed to its highly porous structure, ACC was also infiltrated with S as cathodes, i.e., S-ACC. Electrochemical measurements demonstrated that the S-ACC cathode without the reactivation layer exhibited an initial discharge capacity of 510 mAh/g and quickly dropped to 220 mAh/g after 10 cycles. In comparison, the S-ACC cathode with a bare ACC as the reactivation layer delivered a discharge capacity of 907 mA h/g initially and maintained a capacity of 358 mAh/g after 40 cycles. This increase in capacity was believed being due to the adsorption and reactivation of dissolved lithium polysulfide on the reactivation layer. Very impressively, the S-ACC cathode with an Al_2O_3 -ACC reactivation layer has showed the highest initial discharge capacity of 1136 mAh/g and sustained a capacity of 766 mAh/g after 40 cycles. Obviously, the Al_2O_3 -ACC reactivation layer performed better electrochemical performance than the other two cathodes. SEM and EDX analyses on Al_2O_3 -ACC revealed that a well-defined annular Al distribution did not change during cycling, indicating the stability of ALD- Al_2O_3 coating over ACC. The sulfur distribution formed a distinguishable annulet with a 2 μm wall thickness, coincident with the Al_2O_3 distribution in the fiber. It is apparent that the interaction between polysulfides and Al_2O_3 was stronger than the one between polysulfides and carbon, since there were more sulfur species absorbed in the annular Al_2O_3 region than in the carbon center. In comparison, the SEM and EDX analyses on the bare ACC reactivation layer demonstrated a uniform S distribution throughout the ACC carbon fiber. Comparing the EDX data, the

Al_2O_3 -ACC layer exhibited a higher atomic ratio of S to C (0.09) than the bare ACC (0.03), which indicated that the Al_2O_3 -ACC layer captured more polysulfide species than the bare ACC layer. The EDX results indicated that the polysulfides diffused throughout the whole fiber during cycling, thus, the Al_2O_3 -ACC reactivation layer exhibited the sulfur-collection pattern because of the interaction between polysulfides and Al_2O_3 . A possible mechanism related to the chemisorption of the polysulfide was concluded as the following: the coordination between the lone pair electrons of oxygen groups in Al_2O_3 and Li^+ was effective in attracting polysulfide anions electrostatically. This is also applicable to cyano-groups in PAN (i.e., polyacrylonitrile) that attracted polysulfides through the interaction with Li^+ .^[91] While another mechanism is that Al_2O_3 -ACC has a smaller average pore size of 2.4 nm than the bare ACC (2.6 nm), which was closer to the length of typical polysulfide chains (< 2 nm),^[92] making it easier to adsorb polysulfides within the pores. To verify these hypotheses, a systematic theoretical investigation based on DFT calculations and molecular dynamics simulation might be critical to provide more fundamental insights and understanding on this complex interface design.

3.1.4. 3D Current Collectors

Zhang et al.^[93] recently developed a novel current collector with an ALD surface coating in hope of addressing Li dendrite growth. In their work, a three-dimensional (3D) carbon nanotube sponge (CNTS) was developed as the current collector and coated with a layer of ALD- Al_2O_3 protection film.^[93] It was found that the ALD-coated CNTS not only enabled a homogenous Li^+ nucleation and distribution, but also helped facilitate the Li^+ diffusion more effectively to suppress Li dendrite growth, ascribed to its high specific surface area (300–400 m^2/g), high porosity of > 99%, and high pore volume of 0.83–1.00 cm^3/g .^[94] The thin ALD- Al_2O_3 layer was deposited at 150 °C using TMA and H₂O as precursors, acting as an indispensable artificial SEI to provide a protecting interface between Li metal anode and electrolyte, which significantly enhances the chemical stability and mechanical strength of the Li anode. The 3D ALD- Al_2O_3 coated CNTS could facilitate Li deposition homogeneously and therefore ensure a dendrite-free Li metal anode. Thus, the 3D CNTS was more beneficial than the traditional planar Cu substrate. The latter is prone to form Li dendrites. In comparison to the bare porous CNTS, the ALD-coated CNTS was also interconnected. In the study, Li was first electrodeposited on the 3D ALD-CNTS and the planar Cu at 10 and 18 mAh/cm², respectively, to form the SEI and to provide a Li source for the subsequent cycling. The current collectors after Li deposition were signified as Li@ALD-CNTS and Li@planar Cu, respectively. The cells were subjected to galvanostatic stripping/plating at either 1 or 3 mA/cm² at the same capacity of 1 mAh/cm². At 1.0 mA/cm², the cell using Li@ALD-CNTS indicated a steady and flat voltage profile in the range of 16–30 mV for 100 h of cycling. In contrast, the cell using Li@planar Cu electrode exhibited a fluctuated voltage profile. The over-

potential was 60 mV initially, but increased to 380 mV immediately after cycling 66 h, probably due to the Li dendrites growth and SEI aggravation. At a higher current density of 3.0 mA/cm², the Li@ALD-CNTS exhibited an overpotential of 36 mV initially and a steady cycling performance over 60 h. In comparison, the Li@planar Cu delivered a much higher initial overpotential of 70 mV and failed after cycling 29 h. This failure was probably caused by the continuous consumption of Li metal and formation of the unstable SEI. To investigate the details of the microstructures, the morphologies of Li@ALD-CNTS and Li@planar Cu were tested at 1.0 mA/cm² with different deposition capacities. At 2 mAh/cm², mossy Li dendrites with diameters of 1–5 µm were observed in the Li@planar Cu sample. The surface irregularities of the planar Cu became more prominent at a higher capacity of 10 mAh/cm². To the contrary, the structure of the Li@ALD-CNTS remained to be porous and had no significant changes in morphologies. These all indicate that the ALD-CNTS could greatly mitigate the Li dendritic growth at the nucleation stage by reducing the effective current density and generating a uniform coating on the CNTS surface. Cycling stability of the cells were studied by comparing the CE of Li@ALD-CNTS and Li@Cu electrodes. CE were tested by plating at 2 mAh/cm² and then stripping to a voltage cutoff of 1.0 V at 1 mA/cm². In the study,^[93] it was observed that the CE of Li@planar Cu decreased dramatically from the beginning, fluctuated significantly in 20 cycles, and then ended with 40.2% at the 50th cycle. In contrast, the Li@ALD-CNTS electrode delivered an improved CE of 90.3% during the 10th cycle and kept constantly at 92.4% after 80 cycles. These evidences strongly suggested that ALD-CNTS current collector was effective in stabilizing Li metal anodes and the conformal ALD Al₂O₃ layer served as a robust artificial SEI to enhance the Li electrochemical behavior and inhibit Li dendrites.

3.2. Surface Coating via MLD

3.2.1. S Cathodes

Along with the ALD coatings discussed above, recently MLD as a sister technique has also been used for organic or organic-inorganic hybrid materials for improved Li–S batteries. Li et al.^[95] applied a MLD alucone film in Li–S batteries, in which TMA and EG (i.e., ethylene glycol) were adopted as the precursors. At 100 °C, as illustrated in Figure 16(a),^[95] the alucone MLD process proceeded in two half reactions for one cycle. In their work, the alucone films were applied on the carbon/sulfur (i.e., C/S) cathodes by varying MLD cycles of 2, 5, 10 and 20. In order to evaluate the effect of the alucone film on improving the performance of sulfur cathodes, the researchers investigated the electrochemical behavior of the C/S cathodes with or without the alucone coatings in an ether-based electrolyte (i.e., 1 M LiTFSI in 1:1 DOL/DME). For a typical Li–S battery, the redox process usually exhibits two discharge potential plateaus at 2.3 and 2.1 V, respectively, and one charge voltage plateau at 2.4 V. The bare C/S cathode exhibited an obvious overcharge effect in its voltage profile, due to the

“shuttle effect”. This accounted for the low CE during cycling process.^[96] The 5-cycle alucone coated C/S cathode in the work^[95] showed flat discharge and charge potential plateaus, indicating the high reversibility of the Li–S redox reaction. This suggested the effectiveness of the alucone film in mitigating the “shuttle effect”. However, a much thicker MLD layer could limit the performance of C/S cathodes. In this study,^[95] the 10- and 20-cycle alucone-coated C/S cathodes exhibited much higher potential polarization, indicating limited electrical conductivity and low sulfur reactivity. The cyclability of the bare C/S and the alucone coated C/S cathodes were examined. Li et al.^[95] revealed that the bare C/S cathode delivered an initial discharge capacity of 1400 mAh/g but faded to 310 mA/h after 100 cycles. The 2-cycle alucone MLD coated C/S cathode exhibited a capacity of 1300 mAh/g initially and dropped to 400 mAh/g in 100 cycles. The 5-cycle alucone MLD coated C/S cathode, in comparison, yielded an initial capacity of 1200 mAh/g and maintained a higher capacity of 710 mAh/g after 100 cycles. However, the 10-cycle alucone MLD coated C/S cathode started from an initial capacity of 1155 mAh/g but reduced to 600 mAh/g after 100 cycles. This might be attributed to a thick alucone coating^[62] that has limited the sulfur utilization and posed higher polarization at interface. Therefore, the alucone MLD coated C/S cathodes showed better performance over the bare C/S cathode, specifically >90% vs. 70–80% in CE. The morphology of the bare C/S and alucone coated C/S cathodes were also compared before and after cell cycling (see Figure 16(b)–(d)). Before cell cycling, the bare and alucone-coated sulfur cathodes showed agglomerated nanoparticles within sizes ranging from 40 to 60 nm (see Figure 16(b,d)). After cell cycling, the bare C/S electrode was covered completely by Li–S battery’s discharge products, due to the repeating dissolution and deposition of lithium polysulfides (see Figure 16(c)). The poor performance of the bare C/S electrode was mainly caused by the uncontrolled lithium polysulfide shuttle effect and the decreased sulfur reversibility.^[29,36,97] In contrast, the alucone coated C/S cathode exhibited much less discharge products on its surface (see Figure 16(e)), suggesting that the alucone coating was beneficial to restrain the polysulfides from dissolution and its shuttling. Previous studies have also demonstrated the effects of ALD-Al₂O₃ coatings in improving the performance of C/S cathodes.^[6,64–65,90,98] In their study, Li et al.^[95] further compared the cyclability of the bare, ALD-Al₂O₃ coated, and MLD-alucone coated C/S cathodes at 160 mA/g. They revealed that the MLD-alucone coated C/S cathode enabled the best stability and cyclability, achieving a capacity of 800 mAh/g after 100 cycles. In comparison, the ALD-Al₂O₃ coated C/S cathode sustained a capacity of 600 mAh/g.

In their subsequent study,^[99] Li et al. studied the protective effect of the MLD alucone coatings in a carbonate electrolyte, i.e., 1 M LiPF₆ in 1:1:1 EC:DEC:EMC (ethyl – methyl carbonate). Li et al.^[99] demonstrated that the MLD alucone coatings enabled the coated C/S cathodes to achieve improved electrochemical performance in the traditional carbonate electrolyte. SEM images (see Figure 16(f,g)) showed no evident changes with the 10-cycle MLD alucone-coated C/S cathode, compared to

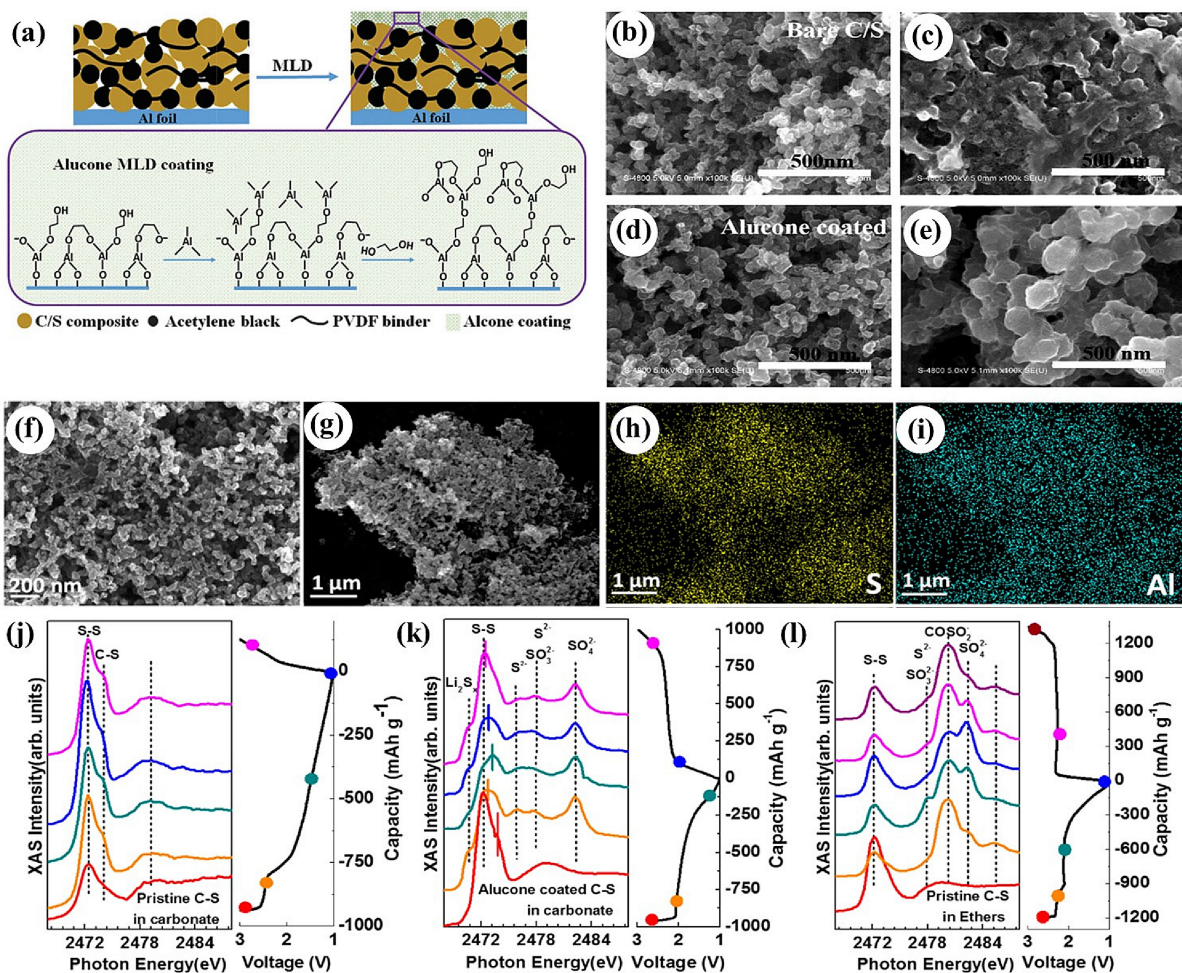


Figure 16. (a) Schematic illustration of alucone MLD thin film formation as a coating layer applied on a C/S cathode. The self-limiting reaction is proceeded with two precursors to produce a layer-by-layer inorganic-organic hybrid composite. FE-SEM images of the bare C/S electrode (b) before and (c) after cycling, and images of the alucone coated C/S electrode (d) before and (e) after cycling.^[95] Reprinted (adapted) with permission from ref. 95. Copyright (2014) Elsevier. (f–g) FE-SEM images of alucone coated C/S electrode and (h–i) EDX elemental mapping of (g). Sulfur K-edge spectra of C/S electrodes at discharge-charge steps: (j) pristine C/S with a carbonate electrolyte, (k) alucone coated C/S with a carbonate electrolyte, and (l) pristine C/S with an ether electrolyte.^[99] Reprinted (adapted) with permission from ref. 99. Copyright (2016) American Chemical Society.

the bare C/S cathode. EDX results (see Figure 16(h,i)) confirmed a uniform alucone film over the C/S cathode. The pristine C/S cathode showed a discharge capacity of 940 mAh/g initially, which faded to 159 mAh/g after 2 cycles and dropped to 98 mAh/g after 100 cycles. This implied the presence of an irreversible electrochemical process. In contrast, the alucone coated C/S cathode exhibited an initial capacity of 912 mAh/g, and sustained a capacity of 429 mAh/g after 100 cycles. In addition, the pristine C/S cathode in the carbonate electrolyte only exhibited a single discharge voltage peak at 2.5 V in the first cycle and without peaks in the following cycles, indicating the generation of long chain lithium polysulfides.^[100] In contrast, the alucone coated C/S cathode delivered the well-defined potential plateaus and a larger voltage gap of 1.5–2.5 V between the cathodic and anodic peaks,^[20c,101] indicating an alternative reaction route as well as higher internal resistance.^[102] To test the thermal stability of the electrolyte/MLD film interface, cycling performance of the alucone MLD coated C–S cathode in the carbonate and ether electrolytes was inves-

tigated at an elevated temperature of 55 °C.^[99] In the carbonate-based electrolyte, the alucone coated C/S cathode exhibited a higher capacity and longer cycle life. The capacity was 1055 mAh/g initially, kept constantly at 661 mA h/g after 50 cycles and maintained at 573 mAh/g after 300 cycles. In the ether electrolyte, the alucone coated C/S cathode delivered a capacity of 1500 mAh/g initially. However, the alucone-coated C/S cathode in the ether electrolyte decreased significantly and failed in 100 cycles. It was believed being due to the low flash point of the ether solvents of DOL and DME (<2 °C). This also posed an important safety concern for the operation of Li–S battery at high temperature such as 55 °C.

To study the underlying mechanism of interaction of sulfide/polysulfide with alucone MLD coating interface, S K-edge of XAS (i.e., X-ray adsorption spectroscopy) data was measured (see Figure 16(j,k)) and summarized in Table 3. In the carbonate electrolyte, the pristine C/S cathode only exhibited one peak of S K-edge at about 2474.0 eV, assigned to $S_x-C_n-C=O$ ^[100,103] probably formed by the chemical reaction between

Table 3. Summary of peak values in S K-edge spectra.

peak /eV		peak /eV	
2472.2	S 1s→S–S π*	2474.0	S _x –Cn–C=O ⁻
2476.2	S 1s→Li ₂ S σ* and or S ²⁻ σ*	2473.6	C–S
2480.5	S 1s→COSO ₂ ⁻ σ*	2470.2, 2472	S _n ²⁻
2482.3	S 1s→SO ₄ ²⁻ σ*	2470.8, 2473.7	Li ₂ S

polysulfide and carbonate solvents (see Figure 16(j)). This subsequently led to electrolyte decomposition^[100] and resulted in the failure of the pristine C/S cathode. Prior to cell cycling, the peak of the alucone-coated C/S cathode at 2473.6 eV was assigned to C–S bond (see Figure 16(k)). This might be related to chemisorption of elemental sulfur on the alucone MLD coating. During the discharge-charging process, the S–S peak of the alucone-coated C/S cathode shifted from 2472.2 to 2473.4 eV and then shifted back to 2472.2 eV, which might be a signature of the reversible redox process between elemental sulfur and polysulfides. In S K-edge spectra of the pristine C/S cathode with the ether electrolyte, there was no shift to the peak at 2472.2 eV, suggesting that there were some severe dissolution and shuttle behaviors of polysulfides during the discharge-charge process (see Figure 16(l)). The XAS data of the three samples suggested that both sulfide and polysulfide species were sensitive to the cathode interface and electrolytes. In particular, MLD coatings could be an effective solution to the issues.

3.2.2. Li Metal Anode

Besides the afore-discussed efforts devoted to sulfur cathodes with MLD coatings, MLD has appeared for engineering Li metal anode. In order to mitigate the parasitic reactions between lithium and electrolyte, and to inhibit dendritic growth, Chen et al.^[104] recently deposited a conformal alucone film on Li surface at 150 °C using EG and TMA as precursors (see Figure 17(a)). The alucone films on Li metal surface were controlled at 3 and 6 nm by varying MLD cycles. To demonstrate the conformal MLD alucone coating, Chen et al.^[104] deposited a 10 nm alucone layer at 150 °C onto 100 nm SiO₂ nanospheres (see Figure 17(b)). Apparently, the MLD alucone coating was smooth, uniform, and conformal. The voltage profiles of the symmetric Li/Li cells with and without 6-nm alucone coating were measured at 1.0 mA/cm² and 1.0 mAh/cm² in a 10 μL carbonate electrolyte. The bare symmetric cell delivered higher polarization over the first 10 cycles and an unstable voltage profile. This might be caused by the morphological changes of Li surface during stripping/plating, leading to a continuously growing thick SEI layer. In contrast, the 6-nm MLD alucone coated symmetric cell showed a much more stable voltage profile. The researchers postulated that the stable voltage profile should be due to a stable and uniform SEI layer, ascribed to the alucone coating. The bare Li/Li cell failed at about 158 h, while the alucone-coated cell remained a stable operation. Chen et al.^[104] also investigated the Li stripping/plating behavior in the bare and alucone-coated Li/Li symmet-

ric cells at 1.0 mA/cm² and 1.0 mAh/cm² (see Figure 17(c)). Compared to the bare symmetric cell, the alucone-coated Li/Li cell showed dramatically improved cyclability. Chen et al.^[104] also studied CE at 0.4 mA/cm² for the bare Li/Cu and alucone protected Li/Cu cells. The bare Li/Cu cell sustained a high CE of 99.5% after 54 cycles but failed in 60 cycles, whereas the alucone protected Li/Cu persisted a high CE of 99.5% for over 160 cycles. This might indicate that the alucone coating has significantly inhibited the dendrite formation. Chen et al.^[104] also assembled the alucone-coated lithium into Li–S full cells using a high sulfur loading S cathode (5 mg/cm²). The cycling performance of the bare Li/S and 6-nm alucone-coated Li/S cells was conducted at 1 mA/cm² (see Figure 17(d)). Capacity fluctuations of the cells were attributed to the thick sulfur laminates. The bare Li–S cell maintained the capacity at 471.6 mAh/g after 140 cycles, while the 6-nm alucone protected Li–S showed a higher capacity of 657.7 mAh/g. The discharge-charge profiles (see Figure 17(e)) showed that the second discharge plateau of 1.85 V was much lower than the expected value (2.1 V) related to the reduction from high-order polysulfides to low-order polysulfides, indicating a voltage polarization for both cells due to the large impedance of the sulfur electrodes. The bare Li–S cell showed a larger overpotential, i.e., 0.5 V versus 0.46 V for the alucone-coated Li–S cell. These are related to the SEI formation and the deposition of polysulfides the bare and MLD-coated Li anodes. Apparently, the alucone coating provided an effective method for high-performance Li anodes.

Almost at the same time, Zhao et al.^[105] conducted a similar work, in which alucone films were deposited on Li metal for different cycles (5, 10, 25 and 50) at 120 °C using TMA and EG as precursors. Correspondingly, the controllable thicknesses were 2.5, 5, 10 and 25 nm, respectively (i.e., Li@5Alucone, Li@10Alucone, Li@25Alucone and Li@50Alucone). Zhao et al.^[105] first investigated the cycling performance of the bare Li and alucone-coated Li in symmetric cells with the ether-based electrolyte (1 M LiTFSI in DOL/DME, 1:1 v/v, 1 wt% LiNO₃). At 3 mA/cm² (see Figure 18(a)), the bare Li foil delivered an overpotential of 50 mV initially, which changed significantly to 120 mV after 50 cycles and maintained at 80 mV for up to 100 cycles. In comparison, Li@10Alucone exhibited an initial overpotential of 100 mV, possibly attributed to the formation of an ionically conductive SEI film between the alucone and the Li. Then, the overpotential decreased to 40 mV after the first few cycles and maintained at 50 mV until 100 cycles. It needs to point out that the Li@10Alucone actually could work for more than 500 cycles (500 h) without any short circuit. Using a higher current density of 5 mA/cm² (see Figure 18(b)), the bare Li delivered an initial overpotential of 80 mV in the symmetric cell. The overpotential increased suddenly to 160 mV after 20 cycles, followed by fluctuations in overpotential voltage. In contrast, the Li@10Alucone showed an overpotential of 100 mV initially and then persisted a stable voltage of 70 mV over 100 cycles. Zhao et al.^[105] further investigated the performance of Li–S full cells through pairing the alucone coated Li anode with a C/S cathode in an ether electrolyte. Using the bare Li anode, the Li–S cell exhibited a capacity fade, possibly due to the dissolved

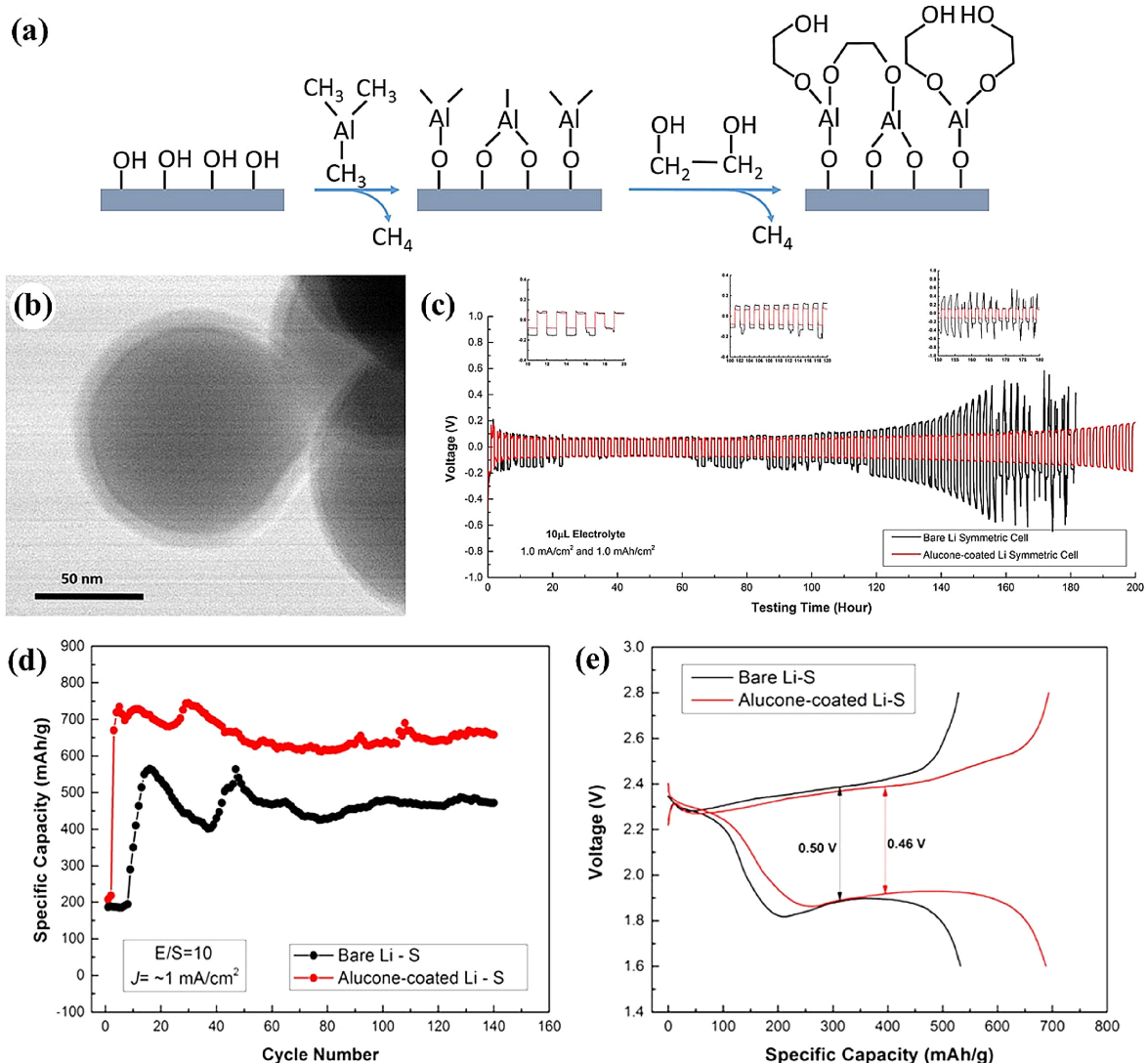


Figure 17. (a) Schematic illustration of the first cycle of alucone MLD beginning with a hydroxylated surface. (b) Transmission electron microscopy (TEM) image of molecular-layer-deposited alucone film on 100 nm SiO₂ nanospheres. (c) Li stripping/plating in different symmetric cells with 10 μL carbonate electrolyte at 1.0 mA/cm² up to a capacity of 1.0 mAh/cm². Alucone on Li is ~6 nm. (d) Cycling performance of Li–S batteries encompassing bare Li or alucone-coated Li with sulfur mass loading of ~5 mg/cm² and an electrolyte volume-to-sulfur mass ratio (E/S, mL/g) of 10 at 0.1 C. (e) Voltage versus capacity profile at the 20th cycle.^[104] Reprinted (adapted) with permission from ref. 104. Copyright (2018) American Chemical Society.

lithium polysulfides and the generation of Li₂S. Using the alucone-coated Li anode, the Li–S cell stabilized in 10 cycles, and the C/S cathode delivered a high capacity (711 mAh/cm²) and CE (95 %) after 100 cycles. Therefore, the alucone coating could prolong the cell life and realize better sulfur utilization by preventing the interaction between polysulfide and Li. SEM observations were conducted on the bare lithium and 5-nm alucone-coated lithium before and after cycling, respectively. Before cycling, no obvious morphological changes were detected between bare Li (see Figure 18(c1,c2)) and the alucone coated Li (see Figure 18(c3, c4)). After 30 plating/stripping cycles, the bare Li anode was observed with a rough surface with Li dendrites (see Figure 18(c5, c6)). However, the alucone-coated Li anode only showed a nodule-like structure with round-shaped edges (see Figure 18 (c7, c8)). The enlarged dimension of nodule-like dendrites could effectively suppress

them from penetrating the separator. In addition, Zhao et al.^[105] also investigated the electrochemical behaviors of the bare Li and the alucone-coated Li anodes in a carbonate-based electrolyte (i.e., 1 M LiPF₆ in 1:1:1 EC:EDC:EMC). They discovered that the bare Li foil exhibited fluctuated voltage profile, which increased dramatically after 300 h cycling. This indicates the continuous increase of resistance and the presence of short circuit. In contrast, the alucone coated Li electrodes were more stable in their voltage profiles. Zhao et al.^[105] found that the Li@50Alucone performed the best in all the symmetric cells, including the bare Li, Li@10Alucone, Li@25Alucone, and Li@50Alucone. Therefore, the alucone coatings were effective in protecting Li anode from reacting with both the ether- and carbonate-based electrolytes. In particular, the optimal thickness of the alucone layer varies with electrolytes. Specifically, the optimal thickness is 10 MLD alucone cycles (5 nm) for the

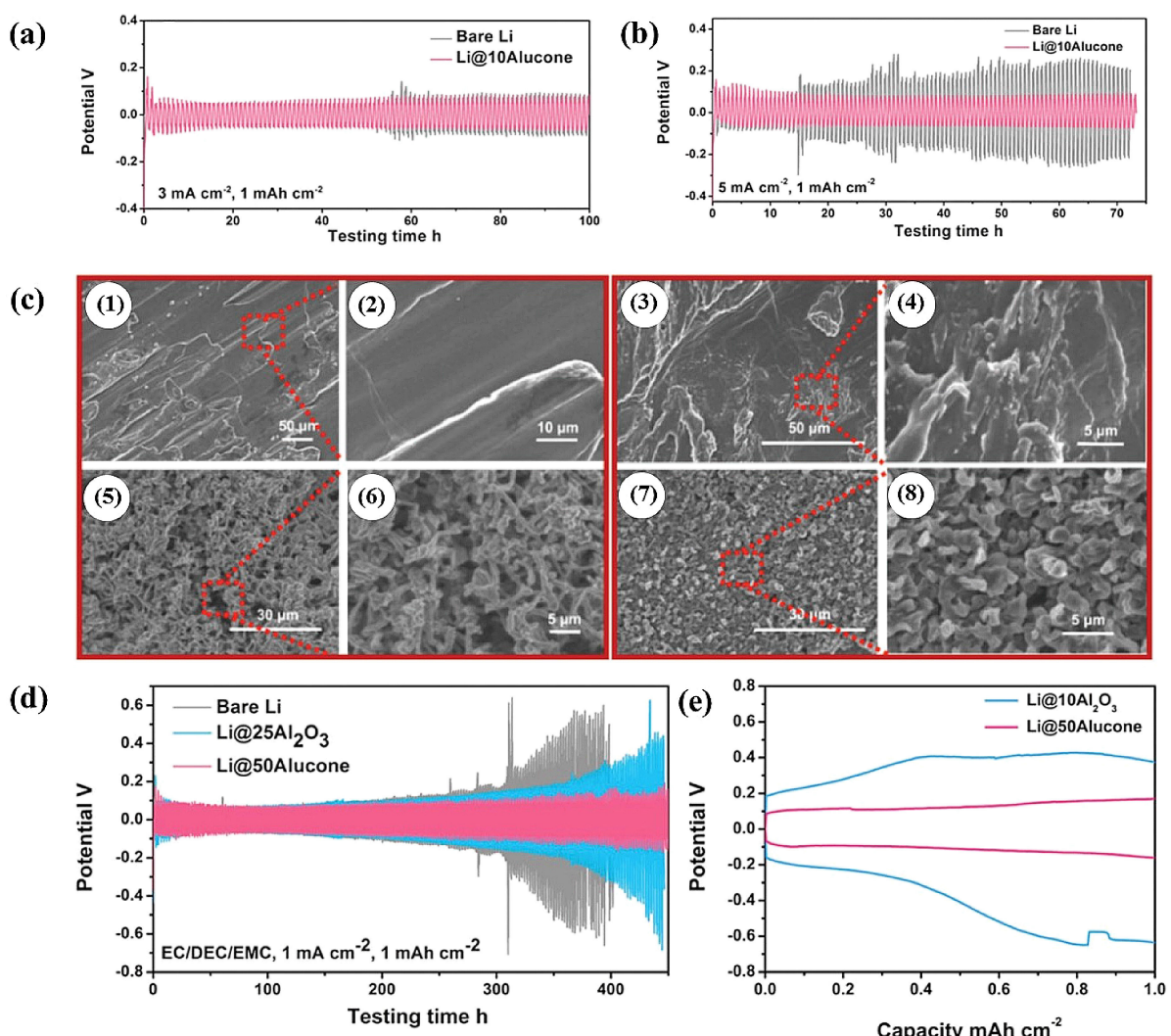


Figure 18. (a) Comparison of the cycling stability of the Li@10Alucone cycles and the bare Li foil at a current density of 3 mA/cm² in DOL/DME electrolyte. (b) Comparison of the cycling stability of the Li@10Alucone cycles and the bare Li foil at a current density of 5 mA/cm² in DOL/DME electrolyte. (c) Top-view SEM images of (1, 2) the bare Li and (3, 4) Li@10Alucone cycles. Top-view SEM images of (5, 6) the bare Li and (7, 8) Li@10Alucone after 30 cycles of stripping/plating in DOL/DME electrolyte at a current density of 3 mA/cm². The amount of Li cycled was 1 mAh/cm². (d) Comparison of cycling performance between the bare Li, Li@25Al₂O₃, and Li@50Alucone in EC/DEC/EMC electrolyte at the current density of 1 mA/cm². (e) Voltage profiles of Li@50Alucone and Li@25Al₂O₃ after 190 cycles at the current density of 1 mA/cm² in EC/DEC/EMC electrolyte.^[105] Reprinted (adapted) with permission from ref. 105. Copyright (2018) John Wiley and Sons.

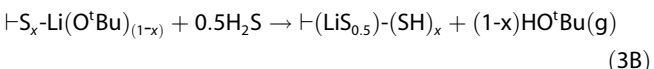
ether-based electrolyte while 50 MLD alucone cycles (25 nm) for carbonate-based electrolyte. Zhao et al.^[105] further conducted a comparative study for clarifying the effects of ALD Al₂O₃ and MLD alucone coatings. In the carbonate electrolyte (see Figure 18(d)), the bare Li only survived for 300 h. In comparison, the Li@25Al₂O₃ (2.5 nm, the optimal thickness) and Li@50Alucone outperformed the bare Li anode. The Li@50Alucone anode showed the best performance with more stable voltage profiles. Thus, it was believed that the alucone layer was robust enough against the electrolyte, mechanically flexible to accommodate repeated Li plating/stripping, and highly ionic conductive for Li⁺ transfer. To facilitate readers, the MLD coatings and their applications are summarized in Table 4.

4. Electrode Designs via ALD

Compared to the many efforts discussed above for ALD and MLD surface coatings, there was only one study reported for electrode designs. In the study, Meng et al.^[88] developed a new ALD process for growing Li₂S films, in which lithium tertbutoxide (LTB) and H₂S were adopted as the precursors (see Figure 19(a)). Using in-situ QCM (quartz crystal microbalance), in-situ QMS (quadrupole mass spectroscopy), and in-situ FTIR (Fourier transform infrared spectroscopy), Meng et al.^[88] made a thorough investigation on the growth mechanism of the Li₂S films. They revealed that the ALD Li₂S enabled a stable growth of 1.1 Å/cycle in the range of 150–300 °C, and described the ALD Li₂S using the following half reactions:

Table 4. MLD alucone coatings on sulfur cathodes and Li metal anodes

MLD coatings	Electrodes	MLD pa-rameters	Electrolytes	Roles of coat-ings	Ref.
Alucone	C/S cath-ode	100 °C, TMA + EG, 2, 5, 10, and 20 cycles	1 M LiTFSI in 1:1 DOL/ DME	(i). Mitigating S shuttling behaviors; (ii). Restraining lithium polysulfides from dissolution.	[95]
	C/S cath-ode	100 °C, TMA + EG, 5.4 nm	1 M LiPF ₆ in 1:1:1 EC:- DEC:EMC 1 M LiTFSI in 1:1 DOL/ DME 1 M LiPF ₆ in 3:7 EC:EMC	(i). Stabilizing the lithium metal anode; (ii) Inhibiting the growth of Li dendrites; (iii). Minimizing the side reaction between Li metal and electrolyte.	[99]
	Li metal	150 °C, TMA + EG, 3 and 6 nm	1 M LiTFSI, 0.18 M Li ₂ S _x , 2 wt% LiNO ₃ in 1:1 DOL/ DME	[104]	
	Li metal	120 °C, TMA + EG, 2.5, 5, 10, and 25 nm	1 M LiTFSI in 1:1 DOL/ DME 1 M LiPF ₆ in 1:1:1 EC:- DEC:EMC	[105]	



where, “–” represents the substrate surface, “g” indicates the gaseous phase. Meng et al.^[88] also confirmed the stoichiometric composition of the ALD Li₂S using XPS (see Figure 19(b)). Furthermore, Meng et al.^[88] deposited the ALD Li₂S films over mesocarbon microbeads (MCMBs, Figure 19(c)) as cathode for electrochemical testing. The resultant MCMB-supported Li₂S (see Figure 19(d)) exhibited an initial discharge capacity of 860 mAh/g, and sustained a capacity of ~800 mAh/g after 36 cycles. Meng et al.^[88] concluded that the suppression of S shuttling was attributed to the functional groups (e.g., –OH, and –CO–) on MCMB surfaces. In addition, the ALD Li₂S nanofilms were beneficial for lithium-ion transfer. In addition, Meng et al.^[88] also demonstrated that this ALD Li₂S process enabled to deposit Li₂S films over Cu foils for exceptional Li₂S cathode showing excellent cyclability and rate capability.

5. Summary and Perspectives

Li–S batteries are very promising, featuring their low cost and extremely high energy density. However, Li–S batteries are suffering from many serious problems associated with their

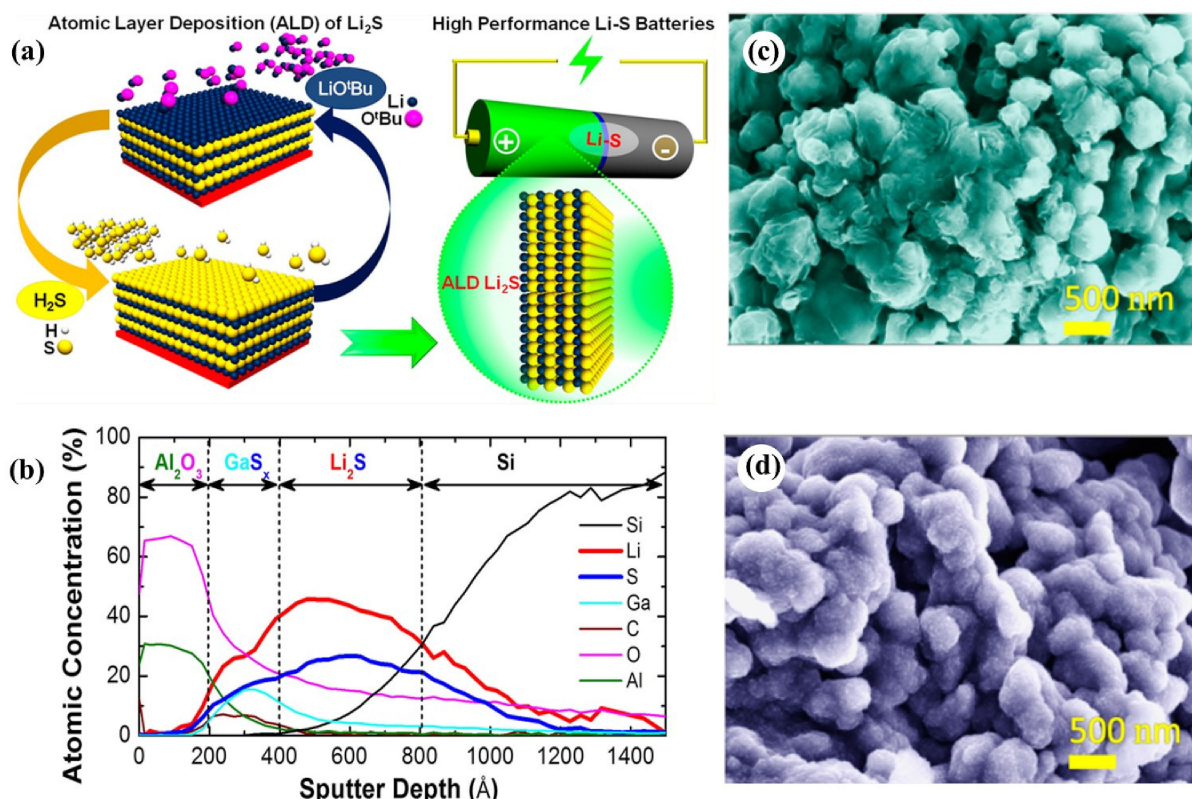


Figure 19. (a) Schematic fabrication of Li₂S via an ALD process. (b) Chemical composition of ALD Li₂S film, atomic concentration versus depth for ALD Li₂S/GaS_x/Al₂O₃ trilayered film prepared using 600 ALD Li₂S cycles, 100 ALD GaS_x cycles, and 100 ALD Al₂O₃ cycles at 200 °C on a Si(100) substrate, measured by XPS depth profiling analysis. SEM images of MCMB particles (c) before and (d) after 700 cycle ALD Li₂S coating.^[88] Reprinted (adapted) with permission from ref. 88. Copyright (2014) American Chemical Society.

anodes, cathodes, as well as other battery components. In addressing these issues, recent studies have shown that both ALD and MLD have emerged as two new thrusts and exhibited many unique benefits. As discussed in the work, various metal oxides^[6,63–66,79,81–83,93] have been applied as surface coatings over S/Li₂S cathodes, serving as absorbents and/or physical barriers to polysulfides. In addition, ALD Al₂O₃ has also been used to form a reactivation layer^[90] and for 3D current collector.^[93] All these demonstrated that ALD was viable for addressing issues of Li–S batteries. It needs to point out that ALD features its precise controllability on the deposited materials. This enables to optimize the coatings' effect and the resultant cathodes' performance. Besides modifying various S cathodes, ALD has also been reported for tackling the issues with lithium metal anodes.^[79,81–83] The studies have demonstrated that the ALD coatings were effective in inhibiting Li dendrites and mitigating SEI formation. Very inspiringly, an ionic conductive coating of Li_xAl_yS has been for the first time reported^[87] and this ionically conductive coating showed exceptional effects in inhibiting lithium dendrites and sustaining high CE. In this direction, more studies are expected from the future research. Along with efforts using ALD, recently there have been MLD efforts reported for Li–S batteries.^[95,99] Alcone films via MLD were applied on S cathodes and Li metal anodes. All the studies so far verified that MLD coatings were effective in mitigating S shuttling and stabilizing lithium metal anodes. In comparison with ALD coatings, MLD coatings are more flexible mechanically. This may underlie their better performance in modifying S cathodes and Li metal anodes. In addition to many modifications via ALD and MLD over S cathodes and Li metal anodes, only one study was reported by ALD for depositing Li₂S cathode.^[88] This work is significant in precisely controlling Li₂S deposition for achieving high electrochemical performance.

All these efforts summarized in this review together have demonstrated that both ALD and MLD are two very unique techniques providing new technical solutions to the challenges exiting in Li–S batteries. Besides surface modifications and electrode designs by ALD and MLD, as discussed in this review, more research efforts may emerge in the direction to search highly ionically conductive lithium conductors. One of the most favorable benefits of ALD and MLD lies in their capability to *in-situ* deposit thin films over cathodes and anodes. This enables to minimize the interfacial issues. In addition to providing new technical solutions, in particular, both ALD and MLD are particularly useful for exploring some fundamental knowledge, owing to their excellent controllability over materials growth. All these features of ALD and MLD are believed being capable of bringing us new excitements in the Li–S battery research.

Acknowledgements

X.M. and Q.S. acknowledge partial support from the Center for Advanced Surface Engineering, under the National Science Foundation Grant No.OIA-1457888 and the Arkansas EPSCoR Program, ASSET III. X. M. also appreciate the financial research support from University of Arkansas, Fayetteville, AR, USA. D.G.

appreciates the financial support from University of Science and Technology Beijing.

Conflict of Interest

The authors declare no conflict of interest.

Keywords: atomic layer deposition • electrochemistry • lithium-sulfur batteries • molecular layer deposition • surface chemistry

- [1] a) A. Avni, M. Blázquez, *Can plant biotechnology help in solving our food and energy shortage in the future?*, Vol. 22, **2011**; b) P. Papon, *Énergie: Science et technique, remparts contre la pénurie?*, **2008**; c) G. Da Rocha, J. Bittencourt de Andrade, A. Lefol Nani Guarieiro, L. Lefol Nani Guarieiro, L. Pereira Ramos, *Chemistry without borders: The energy challenges*, Vol. 36, **2012**; d) A. Nicola, B. Vincenzo, *Angew. Chem. Int. Ed.* **2007**, *46*, 52–66; *Angew. Chem.* **2007**, *119*, 52–67; e) T. R. Cook, D. K. Dogutan, S. Y. Reece, Y. Surendranath, T. S. Teets, D. G. Nocera, *Chem. Rev.* **2010**, *110*, 6474–6502.
- [2] a) Q. Wu, G. Han, *Atmos. Res.* **2015**, *155*, 130–140; b) G. Nicoletti, N. Arcuri, G. Nicoletti, R. Bruno, *Energy Convers. Manage.* **2015**, *89*, 205–213; c) G. Cao, X. Zhang, S. Gong, X. An, Y. Wang, *Chin. Sci. Bull.* **2011**, *56*, 781; d) P. Fontina, I. Diego, D. Javier, *Greenhouse Gas Sci Technol.* **2015**, *5*, 268–276; e) I. S. Modahl, C. Askham, K.-A. Lyng, A. Brekke, *Int J Life Cycle Assess* **2012**, *17*, 932–943.
- [3] a) C. Körner, D. Basler, *Science* **2010**, *327*, 1461–1462; b) D. Aiguo, *WIREs Climate Change* **2011**, *2*, 45–65; c) C. D. Koven, B. Ringeval, P. Friedlingstein, P. Ciais, P. Cadule, D. Khorostyanov, G. Krinner, C. Tarnocai, *Proc. Natl. Acad. Sci. USA* **2011**, *108*, 14769–14774; d) P. M. Cox, R. A. Betts, C. D. Jones, S. A. Spall, I. J. Totterdell, *Nature* **2000**, *408*, 184; e) T. L. Root, J. T. Price, K. R. Hall, S. H. Schneider, C. Rosenzweig, J. A. Pounds, *Nature* **2003**, *421*, 57.
- [4] a) K. Tromly, National Renewable Energy Lab., Golden, CO (US), **2001**; b) I. Dincer, *Renewable Sustainable Energy Rev.* **2000**, *4*, 157–175; c) M. G. Salameh, *Appl. Energy* **2003**, *75*, 33–42.
- [5] G. E. Blomgren, *J. Electrochem. Soc.* **2017**, *164*, A5019–A5025.
- [6] M. P. Yu, W. J. Yuan, C. Li, J. D. Hong, G. Q. Shi, *J. Mater. Chem. A* **2014**, *2*, 7360–7366.
- [7] a) S.-L. Chou, J.-Z. Wang, H.-K. Liu, S.-X. Dou, *J. Phys. Chem. C* **2011**, *115*, 16220–16227; b) H. Maleki, S. A. Hallaj, J. R. Selman, R. B. Dinwiddie, H. Wang, *J. Electrochem. Soc.* **1999**, *146*, 947–954.
- [8] P. G. Bruce, S. A. Freunberger, L. J. Hardwick, J.-M. Tarascon, *Nat. Mater.* **2012**, *11*, 19–29.
- [9] a) J. Li, Z. Du, R. E. Ruther, S. J. AN, L. A. David, K. Hays, M. Wood, N. D. Phillip, Y. Sheng, C. Mao, S. Kalnaus, C. Daniel, D. L. Wood, *JOM* **2017**, *69*, 1484–1496; b) C. Daniel, D. Mohanty, J. Li, D. L. Wood, *AIP Conf. Proc.* **2014**, *1597*, 26–43; c) J. Li, C. Daniel, D. Wood, *J. Power Sources* **2011**, *196*, 2452–2460.
- [10] a) N.-S. Choi, Z. Chen, S. A. Freunberger, X. Ji, Y.-K. Sun, K. Amine, G. Yushin, L. F. Nazar, J. Cho, P. G. Bruce, *Angew. Chem. Int. Ed.* **2012**, *51*, 9994–10024; *Angew. Chem.* **2012**, *124*, 10134–10166; b) M. S. Whittingham, *Chem. Rev.* **2004**, *104*, 4271–4302.
- [11] a) M. Ko, S. Chae, J. Ma, N. Kim, H.-W. Lee, Y. Cui, J. Cho, *Nat. Energy* **2016**, *1*, 16113; b) L. Mai, X. Tian, X. Xu, L. Chang, L. Xu, *Chem. Rev.* **2014**.
- [12] A. Manthiram, Y. Fu, S.-H. Chung, C. Zu, Y.-S. Su, *Chem. Rev.* **2014**, *117*–11787.
- [13] J. Lu, L. Li, J.-B. Park, Y.-K. Sun, F. Wu, K. Amine, *Chem. Rev.* **2014**, *114*, 5611–5640.
- [14] a) S. Zhang, *Front. Energy Res.* **2013**, *1*; b) S. S. Zhang, *ACS Appl. Energy Mater.* **2018**, *1*, 910–920.
- [15] D. Herbert, J. Ulam, United States Patent No. 3043896, **1962**.
- [16] a) R. M. L. Bhaskara, United States Patent No. 3413154A, **1968**; b) D. A. Nole, V. Moss, United States Patent No. 3532543A, **1970**.
- [17] X. Ji, K. T. Lee, L. F. Nazar, *Nat. Mater.* **2009**, *8*, 500.
- [18] a) R. Fang, S. Zhao, Z. Sun, D.-W. Wang, H.-M. Cheng, F. Li, *Adv. Mater.* **2017**, *29*, 1606823; b) X. Liu, J.-Q. Huang, Q. Zhang, L. Mai, *Adv. Mater.* **2017**, *29*, 1601759.

- [19] a) Y. Yang, G. Zheng, Y. Cui, *Chem. Soc. Rev.* **2013**, *42*, 3018–3032; b) J. R. Croy, A. Abouimrane, Z. Zhang, *MRS Bull.* **2014**, *39*, 407–415; c) A. Manthiram, S.-H. Chung, C. Zu, *Adv. Mater.* **2015**, *27*, 1980–2006; d) J. Liang, Z.-H. Sun, F. Li, H.-M. Cheng, *Energy Storage Mater.* **2016**, *2*, 76–106; e) A. Rosenman, E. Markevich, G. Salitra, D. Aurbach, A. Garsuch, F. F. Chesiene, *Adv. Energy Mater.* **2015**, *5*, 1500212.
- [20] a) P. G. Bruce, L. J. Hardwick, K. M. Abraham, *MRS Bull.* **2011**, *36*, 506–512; b) Z. Lin, C. Liang, *J. Mater. Chem. A* **2015**, *3*, 936–958; c) S. Evers, L. F. Nazar, *Acc. Chem. Res.* **2013**, *46*, 1135–1143; d) A. Manthiram, Y. Fu, Y.-S. Su, *Acc. Chem. Res.* **2013**, *46*, 1125–1134; e) L. F. Nazar, M. Cuisinier, Q. Pang, *MRS Bull.* **2014**, *39*, 436–442; f) X. Ji, L. F. Nazar, *J. Mater. Chem.* **2010**, *20*, 9821–9826; g) Z. Li, H. B. Wu, X. W. Lou, *Energy Environ. Sci.* **2016**, *9*, 3061–3070.
- [21] J. A. Ober, in *Mineral Commodity Summaries*, Reston, VA, **2018**, p. 204.
- [22] P. Harrisson, CRU: London, **2016**.
- [23] a) X. Ji, S. Evers, R. Black, L. F. Nazar, *Nat. Commun.* **2011**, *2*, 325; b) J. Wang, S. Y. Chew, Z. W. Zhao, S. Ashraf, D. Wexler, J. Chen, S. H. Ng, S. L. Chou, H. K. Liu, *Carbon* **2008**, *46*, 229–235; c) D. Aurbach, E. Pollak, R. Elazari, G. Salitra, C. S. Kelley, J. Affinito, *J. Electrochem. Soc.* **2009**, *156*, A694–A702.
- [24] a) J. M. Tarascon, M. Armand, *Nature* **2001**, *414*, 359–367; b) M. Winter, in *Zeitschrift für Physikalische Chemie*, Vol. 223, **2009**, p. 1395; c) C. Brissot, M. Rosso, J. N. Chazalviel, S. Lascaud, *J. Power Sources* **1999**, *81*–*82*, 925–929; d) T. Schedlbauer, U. C. Rodehorst, C. Schreiner, H. J. Gores, M. Winter, *Electrochim. Acta* **2013**, *107*, 26–32; e) D. Aurbach, E. Zinigrad, Y. Cohen, H. Teller, *Solid State Ionics* **2002**, *148*, 405–416; f) J. B. Goodenough, Y. Kim, *Chem. Mater.* **2010**, *22*, 587–603; g) Y. S. Cohen, Y. Cohen, D. Aurbach, *J. Phys. Chem. B* **2000**, *104*, 12282–12291.
- [25] a) M. Rosso, C. Brissot, A. Teyssot, M. Dollé, L. Sannier, J.-M. Tarascon, R. Bouchet, S. Lascaud, *Electrochim. Acta* **2006**, *51*, 5334–5340; b) W. Xu, J. Wang, F. Ding, X. Chen, E. Nasibulin, Y. Zhang, J.-G. Zhang, *Energy Environ. Sci.* **2014**, *7*, 513–537.
- [26] S. S. Zhang, *J. Power Sources* **2013**, *231*, 153–162.
- [27] Q. Pang, X. Liang, C. Y. Kwok, L. F. Nazar, *J. Electrochem. Soc.* **2015**, *162*, A2567–A2576.
- [28] M. Barghamadi, A. S. Best, A. I. Bhatt, A. F. Hollenkamp, M. Musameh, R. J. Rees, T. Ruther, *Energy Environ. Sci.* **2014**, *7*, 3902–3920.
- [29] Z. Wei Seh, W. Li, J. J. Cha, G. Zheng, Y. Yang, M. T. McDowell, P.-C. Hsu, Y. Cui, *Nat. Commun.* **2013**, *4*, 1331.
- [30] a) G. Zheng, Y. Yang, J. J. Cha, S. S. Hong, Y. Cui, *Nano Lett.* **2011**, *11*, 4462–4467; b) L. Yuan, H. Yuan, X. Qiu, L. Chen, W. Zhu, *J. Power Sources* **2009**, *189*, 1141–1146; c) L. Ji, M. Rao, S. Aloni, L. Wang, E. J. Cairns, Y. Zhang, *Energy Environ. Sci.* **2011**, *4*, 5053–5059; d) J. Guo, Y. Xu, C. Wang, *Nano Lett.* **2011**, *11*, 4288–4294; e) X. Li, Y. Cao, W. Qi, L. V. Saraf, J. Xiao, Z. Nie, J. Mietek, J.-G. Zhang, B. Schwenzer, J. Liu, *J. Mater. Chem.* **2011**, *21*, 16603–16610; f) B. Zhang, X. Qin, G. R. Li, X. P. Gao, *Energy Environ. Sci.* **2010**, *3*, 1531–1537; g) M.-S. Park, J.-S. Yu, K. J. Kim, G. Jeong, J.-H. Kim, Y.-N. Jo, U. Hwang, S. Kang, T. Woo, Y.-J. Kim, *Phys. Chem. Chem. Phys.* **2012**, *14*, 6796–6804; h) L. Q. Lu, L. J. Lu, Y. Wang, *J. Mater. Chem. A* **2013**, *1*, 9173–9181; i) X. Yang, L. Zhang, F. Zhang, Y. Huang, Y. Chen, *ACS Nano* **2014**, *8*, 5208–5215; j) J.-Z. Wang, L. Lu, M. Choucar, J. A. Stride, X. Xu, H.-K. Liu, *J. Power Sources* **2011**, *196*, 7030–7034; k) D.-W. Wang, Q. Zeng, G. Zhou, L. Yin, F. Li, H.-M. Cheng, I. R. Gentle, G. Q. M. Lu, *J. Mater. Chem. A* **2013**, *1*, 9382–9394.
- [31] S. Evers, T. Yim, L. F. Nazar, *J. Phys. Chem. C* **2012**, *116*, 19653–19658.
- [32] Q. Pang, D. Kundu, M. Cuisinier, L. F. Nazar, *Nat. Commun.* **2014**, *5*, 4759.
- [33] H. Yao, G. Zheng, P.-C. Hsu, D. Kong, J. J. Cha, W. Li, Z. W. Seh, M. T. McDowell, K. Yan, Z. Liang, V. K. Narasimhan, Y. Cui, *Nat. Commun.* **2014**, *5*, 3943.
- [34] Y. J. Choi, B. S. Jung, D. J. Lee, J. H. Jeong, K. W. Kim, H. J. Ahn, K. K. Cho, H. B. Gu, *Phys. Scr.* **2007**, *2007*, 62.
- [35] F. Sun, J. Wang, D. Long, W. Qiao, L. Ling, C. Lv, R. Cai, *J. Mater. Chem. A* **2013**, *1*, 13283–13289.
- [36] Y. Zhang, Y. Zhao, A. Yermukhametova, Z. Bakenov, P. Chen, *J. Mater. Chem. A* **2013**, *1*, 295–301.
- [37] a) J. Hassoun, Y.-K. Sun, B. Scrosati, *J. Power Sources* **2011**, *196*, 343–348; b) T. Takeuchi, H. Kageyama, K. Nakanishi, M. Tabuchi, H. Sakaebe, T. Ohta, H. Senoh, T. Sakai, K. Tatsumi, *J. Electrochem. Soc.* **2010**, *157*, A1196–A1201; c) M. Nagao, A. Hayashi, M. Tatsumisago, *J. Mater. Chem.* **2012**, *22*, 10015–10020; d) A. Hayashi, R. Ohtsubo, T. Ohtomo, F. Mizuno, M. Tatsumisago, *J. Power Sources* **2008**, *183*, 422–426; e) A. Hayashi, R. Ohtsubo, M. Tatsumisago, *Solid State Ionics* **2008**, *179*, 1702–1705.
- [38] a) S. S. Zhang, J. A. Read, *J. Power Sources* **2012**, *200*, 77–82; b) H. Wang, Y. Yang, Y. Liang, J. T. Robinson, Y. Li, A. Jackson, Y. Cui, H. Dai, *Nano Lett.* **2011**, *11*, 2644–2647.
- [39] a) W. Li, Q. Zhang, G. Zheng, Z. W. Seh, H. Yao, Y. Cui, *Understanding the Role of Different Conductive Polymers in Improving the Nanostructured Sulfur Cathode Performance*, Vol. 13, **2013**; b) G.-C. Li, G.-R. Li, S.-H. Ye, X.-P. Gao, *Adv. Energy Mater.* **2012**, *2*, 1238–1245; c) Y. Yang, G. Yu, J. J. Cha, H. Wu, M. Vosgueritchian, Y. Yao, Z. Bao, Y. Cui, *ACS Nano* **2011**, *5*, 9187–9193.
- [40] X. Meng, *J. Mater. Chem. A* **2017**, *5*, 18326–18378.
- [41] a) S. M. George, *Chem. Rev.* **2010**, *110*, 111–131; b) V. Miikkulainen, M. Leskelä, M. Ritala, R. L. Puurunen, *J. Appl. Phys.* **2013**, *113*, 021301; c) R. L. Puurunen, *J. Appl. Phys.* **2005**, *97*, 121301.
- [42] a) L. K. Tae, B. Robert, Y. Taeeun, J. Xulei, N. L. F., *Adv. Energy Mater.* **2012**, *2*, 1490–1496; b) G. Zheng, Q. Zhang, J. J. Cha, Y. Yang, W. Li, Z. W. Seh, Y. Cui, *Nano Lett.* **2013**, *13*, 1265–1270; c) W. Feixiang, K. Hyea, M. Alexandre, L. J. Tae, L. Huan-Ting, Y. Gleb, *Adv. Energy Mater.* **2014**, *4*, 1400196; d) Z. Shu-Mao, Z. Qiang, H. Jia-Qi, L. Xiao-Fei, Z. Wancheng, Z. Meng-Qiang, Q. Wei-Zhong, W. Fei, *Part. Part. Syst. Charact.* **2013**, *30*, 158–165.
- [43] a) X. Meng, *Nanotechnology* **2015**, *26*, 020501; b) X. Meng, *J. Mater. Chem. A* **2017**, *5*, 10127–10149; c) X. Meng, J. W. Elam, *ECS Trans.* **2015**, *69*, 39–57; d) X. Meng, X. Wang, D. Geng, C. Ozgit-Akgun, N. Schneider, J. W. Elam, *Mater. Horiz.* **2017**, *4*, 133–154; e) X. Meng, X.-Q. Yang, X. Sun, *Adv. Mater.* **2012**, *24*, 3589–3615.
- [44] N. P. Dasgupta, X. Meng, J. W. Elam, A. B. Martinson, *Acc. Chem. Res.* **2015**, *48*, 341–348.
- [45] a) M. Yu, A. Wang, Y. Wang, C. Li, G. Shi, *Nanoscale* **2014**, *6*, 11419–11424; b) S. Boukhalfa, K. Evanoff, G. Yushin, *Energy Environ. Sci.* **2012**, *5*, 6872–6879; c) M. N. Liu, X. L. Li, S. K. Karuturi, A. I. Y. Tok, H. J. Fan, *Nanoscale* **2012**, *4*, 1522–1528; d) X. Sun, M. Xie, G. Wang, H. Sun, A. S. Cavanagh, J. J. Travis, S. M. George, J. Lian, *J. Electrochem. Soc.* **2012**, *159*, A364–A369.
- [46] T. Suntola, J. Antson, in *United States Patent*, United States Patent, **1977**, pp. 4,058,430.
- [47] a) B. J. O'Neill, D. H. K. Jackson, J. Lee, C. Canlas, P. C. Stair, C. L. Marshall, J. W. Elam, T. F. Kuech, J. A. Dumesic, G. W. Huber, *ACS Catal.* **2015**, *5*, 1804–1825; b) S. Sun, G. Zhang, N. Gauquelin, N. Chen, J. Zhou, S. Yang, W. Chen, X. Meng, D. Geng, M. N. Banis, R. Li, S. Ye, S. Knights, G. A. Botton, T.-K. Sham, X. Sun, *Sci Rep-Uk* **2013**, *3*, 1775; c) Y. Chen, J. Wang, X. Meng, Y. Zhong, R. Li, X. Sun, S. Ye, S. Knights, *J. Power Sources* **2013**, *238*, 144–149.
- [48] a) T. Wang, Z. Luo, C. Li, J. Gong, *Chem. Soc. Rev.* **2014**, *43*, 7469–7484; b) W. Niu, X. Li, S. K. Karuturi, D. W. Fam, H. Fan, S. Shrestha, L. H. Wong, A. I. Tok, *Nanotechnology* **2015**, *26*, 064001; c) Y. Chen, *Int. J. Hydrogen Energy* **2011**, *36*, 11085–11092.
- [49] S. A. Skoog, J. W. Elam, R. J. Narayan, *Int. Mater. Rev.* **2013**, *58*, 113–129.
- [50] M. Knez, K. Nielsch, L. Niinistö, *Adv. Mater.* **2007**, *19*, 3425–3438.
- [51] a) T. M. Mayer, J. W. Elam, S. M. George, P. G. Kotula, R. S. Goeke, *Appl. Phys. Lett.* **2003**, *82*, 2883–2885; b) O. J. Kilbury, K. S. Barrett, X. W. Fu, J. Yin, D. S. Dinair, C. J. Gump, A. W. Weimer, D. M. King, *Powder Technol.* **2012**, *221*, 26–35; c) A. Pereira, J. L. Palma, J. C. Denardin, J. Escrig, *Nanotechnology* **2016**, *27*, 345709.
- [52] a) H. Kim, *J. Vac. Sci. Technol. B* **2003**, *21*, 2231–2261; b) J. Hämäläinen, M. Ritala, M. Leskelä, *Chem. Mater.* **2014**, *26*, 786–801; c) B. S. Lim, A. Rahtu, R. G. Gordon, *Nat. Mater.* **2003**, *2*, 749–754.
- [53] C. Reitz, B. Breitung, A. Schneider, D. Wang, M. von der Lehr, T. Leichtweiss, J. Janek, H. Hahn, T. Brezesinski, *ACS Appl. Mater. Interfaces* **2016**, *8*, 10274–10282.
- [54] a) M. Putkonen, A. Szeghalmi, E. Pippel, M. Knez, *J. Mater. Chem.* **2011**, *21*, 14461–14465; b) M. Yliilammi, T. Ranta-aho, *J. Electrochem. Soc.* **1994**, *141*, 1278–1284.
- [55] a) C. Platzer-Björkman, T. Törndahl, D. Abou-Ras, J. Malmström, J. Kessler, L. Stolt, *J. Appl. Phys.* **2006**, *100*, 044506; b) E. Thimsen, S. C. Riha, S. V. Baryshev, A. B. F. Martinson, J. W. Elam, M. J. Pellin, *Chem. Mater.* **2012**, *24*, 3188–3196; c) C. Bugot, C. Broussillon, A. Sorba, L. Parisi, N. Schneider, D. Lincot, F. Donsanti, *IEEE PVSC-42*, **2015**, 1–6.
- [56] a) R. W. Johnson, A. Hultqvist, S. F. Bent, *Mater. Today* **2014**, *17*, 236–246; b) J. S. Ponraj, G. Attolini, M. Bosi, *Crit. Rev. Solid State Sci.* **2013**, *38*, 203–233; c) T. Tynell, M. Karppinen, *Semicond. Sci. Technol.* **2014**, *29*, 043001; d) E. Riyanto, E. Rijanto, B. Prawara, *A Review of Atomic Layer Deposition for Nanoscale Devices*, Vol. 3, **2012**; e) D. Nazarov, N. Bobrysheva, O. Osmolovskaya, M. Osmolovsky, V. Smirnov, *Rev. Adv. Mater. Sci.* **2015**, *40*, 262–275.

- [57] a) T. Yoshimura, S. Tatsuura, W. Sotoyama, *Appl. Phys. Lett.* **1991**, *59*, 482–484; b) T. Yoshimura, S. Tatsuura, W. Sotoyama, A. Matsuura, T. Hayano, *Appl. Phys. Lett.* **1992**, *60*, 268–270.
- [58] a) P. W. Loscutoff, H. Zhou, S. B. Clendenning, S. F. Bent, *ACS Nano* **2010**, *4*, 331–341; b) A. Kim, M. A. Filler, S. Kim, S. F. Bent, *J. Am. Chem. Soc.* **2005**, *127*, 6123–6132; c) N. M. Adamczyk, A. A. Dameron, S. M. George, *Langmuir* **2008**, *24*, 2081–2089; d) Y. Du, S. M. George, *J. Phys. Chem. C* **2007**, *111*, 8509–8517; e) M. Putkonen, J. Harjuoja, T. Sajavaara, L. Niinisto, *J. Mater. Chem.* **2007**, *17*, 664–669; f) P. W. Loscutoff, H.-B.-R. Lee, S. F. Bent, *Chem. Mater.* **2010**, *22*, 5563–5569; g) T. Yoshimura, S. Ito, T. Nakayama, K. Matsumoto, *Appl. Phys. Lett.* **2007**, *91*, 033103; h) T. V. Ivanova, P. S. Maydannik, D. C. Cameron, *J. Vac. Sci. Technol. A* **2012**, *30*, 01A121.
- [59] a) S. M. George, B. H. Lee, B. Yoon, A. I. Abdulagatov, R. A. Hall, *J. Nanosci. Nanotechnol.* **2011**, *11*, 7948–7955; b) A. A. Dameron, D. Seghete, B. B. Burton, S. D. Davidson, A. S. Cavanagh, J. A. Bertrand, S. M. George, *Chem. Mater.* **2008**, *20*, 3315–3326; c) B. Yoon, J. L. O’Patchen, D. Seghete, A. S. Cavanagh, S. M. George, *Chem. Vap. Deposition* **2009**, *15*, 112–121; d) A. I. Abdulagatov, R. A. Hall, J. L. Sutherland, B. H. Lee, A. S. Cavanagh, S. M. George, *Chem. Mater.* **2012**, *24*, 2854–2863; e) B. H. Lee, V. R. Anderson, S. M. George, *ACS Appl. Mater. Interfaces* **2014**, *6*, 16880–16887; f) B. Yoon, B. H. Lee, S. M. George, *J. Phys. Chem. C* **2012**, *116*, 24784–24791.
- [60] a) H. Zhou, S. F. Bent, *J. Vac. Sci. Technol. A* **2013**, *31*, 040801; b) K. Gregorczyk, M. Knez, *Prog. Mater. Sci.* **2016**, *75*, 1–37; c) C. Ban, S. M. George, *Adv. Mater. Interfaces* **2016**, 1600762.
- [61] C. Zhu, K. Han, D. Geng, H. Ye, X. Meng, *Electrochim. Acta* **2017**, *251*, 710–728.
- [62] D. M. Piper, J. J. Travis, M. Young, S.-B. Son, S. C. Kim, K. H. Oh, S. M. George, C. Ban, S.-H. Lee, *Adv. Mater.* **2014**, *26*, 1596–1601.
- [63] H. Kim, J. T. Lee, D.-C. Lee, A. Magasinski, W.-i. Cho, G. Yushin, *Adv. Energy Mater.* **2013**, *3*, 1308–1315.
- [64] X. Meng, Y. Liu, Y. Cao, Y. Ren, W. Lu, J. W. Elam, *Adv. Mater. Interfaces* **2017**, 1700096.
- [65] Y. Chen, S. Lu, J. Zhou, X. Wu, W. Qin, O. Ogoke, G. Wu, *J. Mater. Chem. A* **2017**, *5*, 102–112.
- [66] C. Luo, H. Zhu, W. Luo, F. Shen, X. Fan, J. Dai, Y. Liang, C. Wang, L. Hu, *ACS Appl. Mater. Interfaces* **2017**, *9*, 14801–14807.
- [67] M. Yu, A. Wang, F. Tian, H. Song, Y. Wang, C. Li, J.-D. Hong, G. Shi, *Nanoscale* **2015**, *7*, 5292–5298.
- [68] J. A. Rodriguez, A. Maiti, *J. Phys. Chem. B* **2000**, *104*, 3630–3638.
- [69] M. Yu, J. Ma, H. Song, A. Wang, F. Tian, Y. Wang, H. Qiu, R. Wang, *Energy Environ. Sci.* **2016**, *9*, 1495–1503.
- [70] B. Liu, Y. Huang, Y. Wen, L. Du, W. Zeng, Y. Shi, F. Zhang, G. Zhu, X. Xu, Y. Wang, *J. Mater. Chem.* **2012**, *22*, 7484–7491.
- [71] Z. W. Seh, Q. Zhang, W. Li, G. Zheng, H. Yao, Y. Cui, *Chem. Sci.* **2013**, *4*, 3673–3677.
- [72] a) J. Qian, W. A. Henderson, W. Xu, P. Bhattacharya, M. Engelhard, O. Borodin, J.-G. Zhang, *Nat. Commun.* **2015**, *6*; b) Q. Zhang, Y. Wang, Z. W. Seh, Z. Fu, R. Zhang, Y. Cui, *Nano Lett.* **2015**, *15*, 3780–3786.
- [73] R. Carter, L. Oakes, N. Muralidharan, A. P. Cohn, A. Douglas, C. L. Pint, *ACS Appl. Mater. Interfaces* **2017**, *9*, 7185–7192.
- [74] H. Kim, G. Jeong, Y.-U. Kim, J.-H. Kim, C.-M. Park, H.-J. Sohn, *Chem. Soc. Rev.* **2013**, *42*, 9011–9034.
- [75] a) S. M. Choi, I. S. Kang, Y.-K. Sun, J.-H. Song, S.-M. Chung, D.-W. Kim, *J. Power Sources* **2013**, *244*, 363–368; b) F. Wu, J. Qian, R. Chen, J. Lu, L. Li, H. Wu, J. Chen, T. Zhao, Y. Ye, K. Amine, *ACS Appl. Mater. Interfaces* **2014**, *6*, 15542–15549.
- [76] a) N. J. Dudney, *J. Power Sources* **2000**, *89*, 176–179; b) K.-i. Chung, W.-S. Kim, Y.-K. Choi, *J. Electroanal. Chem.* **2004**, *566*, 263–267.
- [77] a) M. Morita, S. Aoki, Y. Matsuda, *Electrochim. Acta* **1992**, *37*, 119–123; b) Y. Matsuda, M. Sekiya, *J. Power Sources* **1999**, *81–82*, 759–761; c) G. H. Lane, P. M. Bayley, B. R. Clare, A. S. Best, D. R. MacFarlane, M. Forsyth, A. F. Hollenkamp, *J. Phys. Chem. C* **2010**, *114*, 21775–21785; d) J.-W. Choi, G. Cheruvally, D.-S. Kim, J.-H. Ahn, K.-W. Kim, H.-J. Ahn, *J. Power Sources* **2008**, *183*, 441–445; e) J. K. Stark, Y. Ding, P. A. Kohl, *J. Electrochem. Soc.* **2011**, *158*, A1100–A1105.
- [78] G. Zheng, S. W. Lee, Z. Liang, H.-W. Lee, K. Yan, H. Yao, H. Wang, W. Li, S. Chu, Y. Cui, *Nat. Nanotechnol.* **2014**, *9*, 618–623.
- [79] A. C. Kozen, C.-F. Lin, A. J. Pearse, M. A. Schroeder, X. Han, L. Hu, S.-B. Lee, G. W. Rubloff, M. Noked, *ACS Nano* **2015**, *9*, 5884–5892.
- [80] K. L. Harrison, K. R. Zavadil, N. T. Hahn, X. Meng, J. W. Elam, A. Leenheer, J.-G. Zhang, K. L. Jungjohann, *ACS Nano* **2017**, *11*, 11194–11205.
- [81] E. Kazyak, K. N. Wood, N. P. Dasgupta, *Chem. Mater.* **2015**, *27*, 6457–6462.
- [82] C.-F. Lin, A. C. Kozen, M. Noked, C. Liu, G. W. Rubloff, *Adv. Mater. Interfaces* **2016**, *3*, 1600426.
- [83] L. Chen, J. G. Connell, A. Nie, Z. Huang, K. R. Zavadil, K. C. Klavetter, Y. Yuan, S. Sharifi-Asl, R. Shahbazian-Yassar, J. A. Libera, A. U. Mane, J. W. Elam, *J. Mater. Chem. A* **2017**, *5*, 12297–12309.
- [84] L. Somerville, J. Bareño, S. Trask, P. Jennings, A. McGordon, C. Lyness, I. Bloom, *J. Power Sources* **2016**, *335*, 189–196.
- [85] J. S. Park, X. B. Meng, J. W. Elam, S. Q. Hao, C. Wolverton, C. Kim, J. Cabana, *Chem. Mater.* **2014**, *26*, 3128–3134.
- [86] S. Hao, C. Wolverton, *J. Phys. Chem. C* **2013**, *117*, 8009–8013.
- [87] Y. Cao, X. Meng, J. W. Elam, *ChemElectroChem* **2016**, *3*, 858–863.
- [88] X. Meng, D. J. Comstock, T. T. Fister, J. W. Elam, *ACS Nano* **2014**, *8*, 10963–10972.
- [89] X. Meng, Y. Cao, J. A. Libera, J. W. Elam, *Chem. Mater.* **2017**, DOI: 10.1021/acs.chemmater.1027b02175.
- [90] X. G. Han, Y. H. Xu, X. Y. Chen, Y. C. Chen, N. Weadock, J. Y. Wan, H. L. Zhu, Y. L. Liu, H. Q. Li, G. Rubloff, C. S. Wang, L. B. Hu, *Nano Energy* **2013**, *2*, 1197–1206.
- [91] J. Guo, Z. Yang, Y. Yu, H. D. Abruna, L. A. Archer, *J. Am. Chem. Soc.* **2013**, *135*, 763–767.
- [92] Y.-S. Su, A. Manthiram, *Nat. Commun.* **2012**, *3*, 1166.
- [93] Y. Zhang, B. Liu, E. Hitz, W. Luo, Y. Yao, Y. Li, J. Dai, C. Chen, Y. Wang, C. Yang, H. Li, L. Hu, *Nano Res.* **2017**, *10*, 1356–1365.
- [94] X. Gui, J. Wei, K. Wang, A. Cao, H. Zhu, Y. Jia, Q. Shu, D. Wu, *Adv. Mater.* **2010**, *22*, 617–621.
- [95] X. Li, A. Lushington, J. Liu, R. Li, X. Sun, *Chem. Commun.* **2014**, *50*, 9757–9760.
- [96] a) H. Jia, J. Wang, F. Lin, C. W. Monroe, J. Yang, Y. NuLi, *Chem. Commun.* **2014**, *50*, 7011–7013; b) S.-H. Chung, A. Manthiram, *Chem. Commun.* **2014**, *50*, 4184–4187; c) C. Wang, H. Chen, W. Dong, J. Ge, W. Lu, X. Wu, L. Guo, L. Chen, *Chem. Commun.* **2014**, *50*, 1202–1204.
- [97] Y. Yang, G. Zheng, Y. Cui, *Energy Environ. Sci.* **2013**, *6*, 1552–1558.
- [98] S. C. Jung, Y.-K. Han, *J. Phys. Chem. Lett.* **2013**, *4*, 2681–2685.
- [99] X. Li, A. Lushington, Q. Sun, W. Xiao, J. Liu, B. Wang, Y. Ye, K. Nie, Y. Hu, Q. Xiao, R. Li, J. Guo, T.-K. Sham, X. Sun, *Nano Lett.* **2016**, *16*, 3545–3549.
- [100] T. Yim, M.-S. Park, J.-S. Yu, K. J. Kim, K. Y. Im, J.-H. Kim, G. Jeong, Y. N. Jo, S.-G. Woo, K. S. Kang, I. Lee, Y.-J. Kim, *Electrochim. Acta* **2013**, *107*, 454–460.
- [101] a) R. Elazari, G. Salitra, A. Garsuch, A. Panchenko, D. Aurbach, *Adv. Mater.* **2011**, *23*, 5641–5644; b) X. Pu, G. Yang, C. Yu, *Adv. Mater.* **2014**, *26*, 7456–7461.
- [102] a) M. Nagao, Y. Imade, H. Narisawa, T. Kobayashi, R. Watanabe, T. Yokoi, T. Tatsumi, R. Kanno, *J. Power Sources* **2013**, *222*, 237–242; b) M. Nagao, A. Hayashi, M. Tatsumisago, *Electrochim. Acta* **2011**, *56*, 6055–6059.
- [103] a) C. Fu, B. M. Wong, K. N. Bozhilov, J. Guo, *Chem. Sci.* **2016**, *7*, 1224–1232; b) M. Vijayakumar, N. Govind, E. Walter, S. D. Burton, A. Shukla, A. Devaraj, J. Xiao, J. Liu, C. Wang, A. Karim, S. Thevuthasan, *Phys. Chem. Chem. Phys.* **2014**, *16*, 10923–10932; c) M. Cuisinier, C. Hart, M. Balasubramanian, A. Garsuch, L. F. Nazar, *Adv. Energy Mater.* **2015**, *5*, 1401801.
- [104] L. Chen, Z. Huang, R. Shahbazian-Yassar, J. A. Libera, K. C. Klavetter, K. R. Zavadil, J. W. Elam, *ACS Appl. Mater. Interfaces* **2018**, *10*, 7043–7051.
- [105] Y. Zhao, L. V. Goncharova, Q. Sun, X. Li, A. Lushington, B. Wang, R. Li, F. Dai, M. Cai, X. Sun, *Small Methods* **2018**, *2*, 1700417.

Manuscript received: April 20, 2018

Version of record online: May 30, 2018